Redox Biology 83 (2025) 103638

Contents lists available at ScienceDirect

Redox Biology

journal homepage: www.elsevier.com/locate/redox

iPSC-derived cardiomyocytes and engineered heart tissues reveal suppressed JAK2/STAT3 signaling in *LMNA*-related emery-dreifuss muscular dystrophy

Hangping Fan [a,b,1], Zongkuai Yang [a,b,1], Hangying Ying [c,1], Jiuxiao Zhao [d], Xiaochen Wang [a,b], Junhao Gong [e], Lingying Li [e], Xujie Liu [e], Tingyu Gong [f,*], Qing Ke [g,**], Lenan Zhuang [d,***], Ping Liang [a,b,****]

[a] *Key Laboratory of Combined Multi-organ Transplantation, Ministry of Public Health, The First Affiliated Hospital, Zhejiang University School of Medicine, Hangzhou, 310003, China*
[b] *Institute of Translational Medicine, Zhejiang University, Hangzhou, 310029, China*
[c] *Department of Cardiology, Sir Run Run Shaw Hospital, Zhejiang University School of Medicine, Hangzhou, 310016, China*
[d] *Department of Veterinary Medicine, College of Animal Sciences, Zhejiang University, Hangzhou, 310058, China*
[e] *Shenzhen Key Laboratory of Cardiovascular Disease, Fuwai Hospital Chinese Academy of Medical Sciences, Shenzhen, 518052, China*
[f] *Shulan International Medical College, Zhejiang Shuren University, Hangzhou, 310015, China*
[g] *Department of Neurology, The First Affiliated Hospital, Zhejiang University School of Medicine, Hangzhou, 310003, China*

ARTICLE INFO

Keywords:
iPSC-CMs
EHTs
JAK2/STAT3 signaling
lamin A/C
EDMD
ROS

ABSTRACT

LMNA mutation related Emery-Dreifuss muscular dystrophy (*LMNA*-related EDMD), is a rare genetic disorder often involving life-threatening cardiac complications. However, the molecular links between *LMNA* mutations and their related EDMD cardiac phenotypes have remained unclear. Here, using EDMD patient-specific and genome-edited induced pluripotent stem cell-derived cardiomyocytes (iPSC-CMs), we link the *LMNA* L204P mutation with the pathogenic phenotypes of arrhythmia and contractile dysfunction. Using multi-omics analysis, we then show that *LMNA* L204P results in decreased chromatin accessibility, leading to the downregulation of *JAK2* in EDMD iPSC-CMs. Mechanistically, JAK2/STAT3 signaling pathway suppression in EDMD iPSC-CMs is shown to cause mitochondrial dysfunction and oxidative stress, ultimately resulting in the above phenotypes. Conversely, pharmacological or genetic activation of JAK2/STAT3 signaling effectively rescues both the arrhythmic and contractile dysfunction phenotypes in EDMD iPSC-CMs via improvements in mitochondrial function. In addition, whilst EDMD engineered heart tissues (EHTs) display dysfunctional contractile force generation, this can also be significantly alleviated by STAT3 activation. Taken together, we present chromatin compartment change-mediated JAK2/STAT3 suppression as a novel mechanism underlying cardiac pathogenic phenotypes in *LMNA*-related EDMD. Our findings indicate that activating the JAK2/STAT3 signaling pathway may hold the potential to serve as a novel therapeutic strategy for this condition.

1. Introduction

Emery-Dreifuss muscular dystrophy (EDMD) is a genetically heterogeneous neuromuscular disorder with an estimated global prevalence of 1:200,000 [1–3]. EDMD patients are characterized by early contractures, slowly progressive muscle wasting and weakness, and cardiomyopathy with conduction block [1–3]. Further confirmation of diagnosis then requires skeletal muscle biopsy and genetic

---

[*] Corresponding author.
[**] Corresponding author.
[***] Corresponding author.
[****] Corresponding author. Key Laboratory of Combined Multi-organ Transplantation, Ministry of Public Health, The First Affiliated Hospital, Zhejiang University School of Medicine, Hangzhou, 310003, China.

E-mail addresses: 11918392@zju.edu.cn (T. Gong), keqing2003@zju.edu.cn (Q. Ke), zhuangln@zju.edu.cn (L. Zhuang), pingliang@zju.edu.cn (P. Liang).

[1] These authors contributed equally to this work.

https://doi.org/10.1016/j.redox.2025.103638
Received 6 March 2025; Received in revised form 9 April 2025; Accepted 14 April 2025

examinations. Groups of genes including *EMD*, *LMNA*, *SYNE1*, *SYNE2*, *FHL1*, *TMEM43*, *SUN1*, *SUN2* and *TTN* have been implicated in EDMD, although their underlying mechanisms are complex and not yet fully elucidated [2].

Cardiac complications among EDMD patients have been strongly highlighted, many of which are life-threatening [3,4]. Some patients experience sudden death without prior cardiac symptoms, especially in EDMD as caused by *LMNA* mutations (*LMNA*-related EDMD) [5]. The *LMNA* gene encodes alternative spliced mRNAs that give rise to lamin A and lamin C. These lamins are then believed to play a pivotal role in the organization of the nuclear envelope (NE) and in defining higher-order chromatin domains [6–8]. Lamins, as type V intermediate filament proteins, possess a conserved tripartite domain structure. This structure includes a central α-helical coiled-coil rod domain flanked by a non-helical N-terminal head domain and an unstructured C-terminal tail domain containing immunoglobulin domains [9]. The central rod domain is responsible for forming coiled-coil dimers as the building blocks of the lamin filaments. These dimers interact laterally to form tetrameric filaments, which then further assemble into a dense meshwork [10]. This meshwork, known as the nuclear lamina, lines the inner nuclear membrane and provides mechanical stability to the nucleus. Nuclear lamina also serves as a scaffold for the binding of transcription of factors and plays a crucial role in maintaining nuclear structure and integrity [7–9,11]. Previous reports show that lamin A/C mutations can affect post-translational modifications (PTMs) such as phosphorylation and SUMOylation, crucial for lamin function and nuclear stability. For example, phosphorylation at specific sites has been shown to be associated with laminopathies, where such *LMNA* mutations are able to disrupt these PTMs and lead to disease progression. Similarly, SUMOylation of lamins has been reported to play a role in cell cycle progression and nuclear organization, where laminopathy mutants may show altered SUMOylation dynamics that also contribute to disease development.

The LINC (Linker of Nucleoskeleton and Cytoskeleton) complex is a crucial structure that spans the NE, connecting the nucleoskeleton to the cytoskeleton and playing a central role in mechanotransduction [12]. Core components of the LINC complex include the SUN domain proteins (SUN1 and SUN2), and KASH domain proteins (nesprins). These interact to form a bridge between inner and outer nuclear membranes [13]. This complex enables the transmission of mechanical forces from the cytoplasm to the nucleus, allowing the cell to sense and respond to mechanical stimuli from its environment [14]. Such mechanotransduction involves the conversion of mechanical signals into biochemical responses where, when cells are subjected to mechanical stresses such as compression or stretching, the LINC complex transmits these forces to the nucleoskeleton including the nuclear lamina and chromatin. This transmission may then lead to changes in the organization of the cytoplasm and the nucleoskeleton [15]. For example, mechanical stress can cause chromatin reorganization, altering its accessibility to transcription factors and thereby affecting gene expression [16]. Additionally, the LINC complex can influence the positioning and movement of the nucleus within the cell, essential for processes such as cell migration and differentiation [12,15]. Signaling pathways can also modulate cytoplasmic reorganization which may have subsequent impact on the nucleoskeleton. For instance, mechanical signals from the extracellular matrix can activate signaling cascades that affect the cytoskeleton, leading to changes in the tension and structure of the nuclear envelope [17]. These changes, in turn, may influence the mechanical properties of the nucleus and its ability to respond to further mechanical stimuli. The interplay between the LINC complex, the cytoskeleton, and the nucleoskeleton therefore represents a dynamic process that allows cells to adapt to their mechanical environment and maintain their structural and functional integrity [12,14,15,18].

Related to this, lamin A/C serves to coordinate genome reprogramming and directly couples mechanotransduction to chromatin through its direct interaction with DNA. This process occurs at lamina-associated domains [19]. In previous studies, *LMNA* haploinsufficiency has been observed to affect the chromatin landscape and induce aberrant gene accessibility in both induced pluripotent stem cell-derived cardiomyocytes (iPSC-CMs) [20,21] and mouse embryo fibroblasts [22]. Meanwhile, lamin A/C has also been identified as a key modulator of mitochondrial function, where disrupted mitochondrial homeostasis, along with unstable mitochondrial DNA and attenuated bioenergetics, has been observed in *LMNA* deficient cells. This may have broad implications for disease progression [23].

The Janus Kinase 2 (JAK2)/Signal Transducer and Activator of Transcription 3 (STAT3) signaling cascade is crucial for transducing cellular signals from the plasma membrane to the nucleus [24], thereby playing a pivotal role in regulating a myriad of biological processes. Upon activation, JAK2 catalyzes the phosphorylation of STAT3, leading to the formation of phosphorylated STAT3 (p-STAT3) [25]. This active form of STAT3 subsequently translocates to the nucleus, where it orchestrates the transcriptional regulation of various genes that are critical for cell survival, differentiation, and proliferation [26]. In the context of cardiomyocyte mitochondria, STAT3 is implicated in modulating mitochondrial respiration, governing mitochondrial apoptosis, and suppressing the opening of mitochondrial permeability transition pores (mPTP) [27–30]. The activation of the JAK2/STAT3 pathway has been recognized for its significant anti-oxidative effects and its role as a key mediator in safeguarding against myocardial ischemia-reperfusion (IR) injury [31–34]. Overexpression of STAT3 preserved complex 1 respiration in an ischemic model was able to reduce the production of reactive oxygen species (ROS), highlighting its cardioprotective effect [28,29].

Here we establish induced pluripotent stem cell-derived cardiomyocyte (iPSC-CM) and engineered heart tissue (EHT) models from a EDMD patient carrying a heterozygous mutation in the *LMNA* gene (c.611T > C, p.L204P). These human-based, patient-specific *in vitro* models were used to characterize the cardiac pathogenic phenotypes of *LMNA*-related EDMD, elucidate the underlying molecular mechanisms, and identify novel therapeutic targets.

2. Materials and methods

2.1. Patient recruitment

3-mm skin punch biopsies were taken from the EDMD patient with informed consent. This study conformed to the principles outlined in the Declaration of Helsinki and was approved by the Ethics Committee of the First Affiliated Hospital, Zhejiang University School of Medicine (IIT20240103B-X2, No. 2024-097).

2.2. Generation of iPSC lines

Somatic reprogramming was used to generate EDMD patient-specific iPSC lines from skin fibroblasts using the CytoTune-iPS 2.0 Sendai Reprogramming Kit, following the manufacturer's instructions (Invitrogen, A16517).

2.3. Single guide RNA (sgRNA) and homology-directed repair (HDR) design for correction of the LMNA L204P mutation

Since the mutation site happens to be located at the first base of the protospacer adjacent motif (PAM) sequence NGG (CGG > TGG), we designed a guide RNA (gRNA) targeting this PAM. This guide sequence was then cloned into PX459 (Addgene: #62988), a spCas9 expression vector with puromycin resistance gene, following Feng Zhang's lab released protocol [35]. The plasmid containing the gRNA cloned into the PX459 vector was named as PX459-L204P. A 100-nucleotide single-stranded oligodeoxynucleotide (ssODN) was designed as the HDR donor template. This ssODN, complementary to the sgRNA strand, contained homology arms flanking the correction site with symmetric extensions [36]. Both the sgRNA (GCAGACCATGAAGGAGGAAC) and

HDR oligos (GCTGCGGCGGGTGGATGCTGAGAACAGGCTGCAGACCATGAAGGAGGAACTGGACTTCCAGAAGAACATCTACAGTGAGGAGCTGCGTGAGACCAAGCGCC) were synthesized by Sangon Biotech (Shanghai, China). For cell nucleofection, one million EDMD iPSCs were dissociated with EDTA and pelleted by centrifugation at 200*g* for 5 min. A total of 5 μg of PX459-L204P/ssODN mixture (1:1 wt ratio) was combined with nucleofection buffer (P3 Primary Cell 4D-Nucleofector™ X Kit) and electroporated into the cell pellets using the CA137 program on the Lonza Nucleofector. 48 h post-nucleofection, cells were selected using 0.5–1.5 μg/ml puromycin for 5 consecutive days. Surviving cell clones were then subcloned and genotyped by PCR and Sanger Sequencing. The forward primer sequences for PCR were 5′-GTAGATGTCCTGACCCCTGC-3′, and the reverse primer sequences were 5′-CAGAATAAGTCTTCTCCAGCTCCTT-3'.

2.4. Cardiac differentiation

The iPSC-CMs were generated using a 2D monolayer differentiation protocol. Briefly, $\sim 10^5$ undifferentiated iPSCs were dissociated and replated into Matrigel-coated 6-well plates. These iPSCs were then cultured and expanded to 85 % confluence before being treated for 2 days with 6 μM CHIR99021 (Axon Medchem, 1386) in RPMI 1640 (Gibco, C11875500BT) with B27 supplement minus insulin (Gibco, A1895601) (RPMI + B27-Insulin) to activate the Wnt signaling pathway. On day 2, cells were placed in RPMI + B27-Insulin without CHIR99021. On days 3–4, cells were treated with 5 μM IWR-1 (Millipore, 681669) to inhibit the Wnt signaling pathway. On days 5–6, cells were removed from IWR-1 treatment and placed into RPMI + B27-Insulin. From day 7 onwards, cells were placed and cultured in RPMI 1640 with B27 supplement containing insulin (Gibco, 17504044) (RPMI + B27+Insulin) until beating was observed. Cells were glucose-starved for 3 days with RPMI + B27+Insulin for purification. Cardiomyocytes obtained 30–40 days after cardiac differentiation were utilized for downstream functional assays.

2.5. Western blot

The iPSC-CMs were detached using TrypLE and then pelleted at 1000 rpm for 5 min at 4 °C. After washing with PBS, the pellets were resuspended in 50–100 μl of lysis buffer. The lysates were placed on ice for 30 min, and the supernatants were then collected after centrifugation at 12,000 rpm for 15 min. Histones were extracted using a histone extraction kit (Proteintech, PK10022) according to the manufacturer's instructions. Cytoplasmic and nuclear extracts were separated using NE-PER™ Nuclear and Cytoplasmic Extraction Reagents (Thermo Scientific, 78833). Protein concentrations were measured using a BCA kit (Pierce, 23227). Western blotting was performed using a standard protocol with the following antibodies: lamin A/C (Abcam, ab108595, 1:1000), phospho-Histone H2A.X Ser139 (Sigma, 05-636-I, 1:1000), Histone H3 (Proteintech, 17168-1-AP, 1:1000), JAK2 (Abcam, ab108596, 1:1000), STAT3 (Proteintech, 60199-1-Ig, 1:1000), Phospho-STAT3 Ser727 (Proteintech, 60479-1-Ig, 1:1000), phospho-STAT3 Tyr705 (Proteintech, 39596, 1:1000), and GAPDH (Abmart, M20006 M, 1:5000). The intensity values for each band were determined as the integrated density (sum of pixel values) within a fixed area using Quantity One software (Bio-Rad).

2.6. Immunofluorescent staining

Cells were fixed with 4 % paraformaldehyde (PFA) (Beyotime Biotechnology, P0099) for 15 min, permeabilized with 0.1 % Triton X-100 (Sangon Biotech, A110694) for 5 min, and blocked with 3 % bovine serum albumin (BSA) (Sigma-Aldrich, A1933) for 1 h. Cells were subsequently stained with appropriate primary antibodies and AlexaFluor conjugated secondary antibodies. Primary antibodies were OCT4 (Cell Signaling Technology, 2750S, 1:200), NANOG (Santa Cruz Biotechnology, sc-33759, 1:200), SSEA-4 (Abcam, ab16287, 1:200), SOX2 (Abcam, ab171380, 1:200), TNNT2 (Abcam, ab45932, 1:500), α-actinin (Abcam, ab9465, 1:500), lamin A/C (Abcam, ab108595, 1:400), STAT3 (Proteintech, 60199-1-Ig, 1:500), phospho-Histone H2A.X Ser139 (Sigma, 05-636-I, 1:1000), MYHC (Proteintech, 22281-1-AP, 1:500) and MyoG (Proteintech, 26762-1-AP, 1:500). Secondary antibodies were AlexaFluor® 594 (Abcam, ab150080, 1:500) and AlexaFluor® 488 (Abcam, ab150113, 1:500). Nuclei were stained with DAPI (Roche Diagnostics, 1023276001, 1 μg/ml). Pictures were taken with 20 × or 60 × objective on confocal microscope (Nikon, A1) using NIS-Elements AR software (Nikon).

2.7. Patch clamp recordings from iPSC-CMs

The iPSC-CMs were mechanically and enzymatically dissociated to obtain single cells. These were seeded on Matrigel-coated glass coverslips. Cells with spontaneous beatings were selected and action potentials were recorded using an EPC-10 patch clamp amplifier (HEKA). Continuous extracellular solution perfusion was achieved using a rapid solution exchanger (Bio-logic Science Instruments, RSC-200). All signals were acquired using PatchMaster software (HEKA) having been filtered at 1 kHz and digitized at 10 kHz. Data analysis was performed using Igor Pro (Wavemetrics) and GraphPad Prism (GraphPad Software). A TC-344C dual channel heating system (Warner Instruments) was used to maintain the temperature at 35.5–37 °C. Tyrode's solution was used as the external solution containing 140 mM NaCl, 5.4 mM KCl, 1 mM $MgCl_2$, 10 mM glucose, 1.8 mM $CaCl_2$, 1.0 mM Na-Pyruvate and 10 mM HEPES (pH 7.4 with NaOH). The internal solution contained 140 mM KCl, 5.0 mM NaCl, 10 mM HEPES, 5 mM Mg-ATP and 5 mM EGTA (pH 7.2 with KOH). Key action potential parameters were quantified including maximal diastolic potential (MDP), overshoot, action potential amplitude (APA), action potential duration at 50 % or 90 % repolarization (APD_{50} and APD_{90}, respectively), maximal upstroke velocity (V_{max}), beating rate, and SD of inter-spike intervals (ISIs). Ventricular-like iPSC-CMs were distinguished based on action potential morphology and action potential parameters (which exhibited a clear plateau phase), larger APA and V_{max} values, negative MDP values, $APD_{30\text{-}40}/APD_{70\text{–}80} > 1.5$, and $APD_{90}/APD_{50} \leq 1.3$.

2.8. IonOptix

The iPSC-CMs were plated in confocal dishes for 3–5 days before the experiments. Cardiomyocyte contractions were recorded under constant superfusion of Tyrode's solution using the Contractility Complete System (IonOptix, Westwood, MA). For this, the recording temperature was maintained at 37 °C using a TC-324 temperature controller (Warner Instruments) and the IonWizard data acquisition and analysis software was opened, with the iPSC-CM contraction recording mode selected. Recording was performed using an IonOptix CCD camera. The cells were stimulated with the Myopacer EP Field stimulator, with parameters of 10 V voltage, 4 ms delay, and 1 Hz stimulation frequency. Cells that beat regularly at the stimulation frequency were selected for contraction recording. The IonWizard data acquisition and analysis software was used for data analysis. After filtering the data, the measurement indices were selected, and various parameters in the “add transient” section of the Marks option were adjusted. The contraction curve to be analyzed was selected, and the Monotonic Transient Analysis and Export buttons selected to export the data.

2.9. RNA sequencing (RNA-Seq)

For RNA-Seq data, raw FASTQ files were filtrated using fastp and aligned to the reference genome (GRCh38) using hisat2 which sorted the alignments and converted them into BAM format. These BAM files were used for quantifying gene expressions via featureCounts. Raw expected counts (featureCount output) were used as input for differentially expressed gene (DEG) analysis. Count files were normalized and analyzed using DESseq2 in R. DEGs were defined with the cutoff set as pvalue $\leq$ 0.05&|log2foldchange|$\geq$1. The obtained upregulated and downregulated DEGs were subjected to DAVID Gene Ontology (GO) analysis to identify enriched Biological Process terms. Generation of heatmaps was facilitated by the R package pheatmap, while volcano and PCA plots were drawn using ggplot2. Default settings were used for all above analyses.

2.10. *Comet assay*

DNA damage was detected using a comet assay kit (Biogradetech, D-AKE3040). According to the instructions, the cells were mixed with melted agarose and added onto a slide. The cell membrane was then disrupted with a lysis solution, and the DNA uncoiled using an alkaline solution. Finally, the sample was electrophoresed. Under the influence of the electric field, the macromolecular DNA in normal cells migrated a shorter distance, with intact DNA remaining within the cell nucleus, while fragmented DNA migrated out of the nucleus. After staining with PI, the samples were observed under a Zeiss inverted fluorescence microscope (AXIO Observer A1). Images were finally analyzed using CASP Comet Analysis Software.

2.11. *Transmission electron microscopy*

The iPSC-CMs were dissociated with Tripsin-EDTA (Gibco, 25200072), scraped into a 1.5-ml microcentrifuge tube, centrifuged, and then fixed with 2.5 % glutaraldehyde (Sigma-Aldrich, G5882) in 0.1 M phosphate buffer overnight at 4 °C. Specimens were post-fixed with 1 % OsO_4 in phosphate buffer, dehydrated by a graded series of ethyl-alcohol for 15–20 min at each step, and then transferred to absolute acetone for 20 min. Thereafter, specimens were placed in 1:1 mixture of absolute acetone and final spur resin mixture for 1 h at room temperature, transferred to 1:3 mixture of absolute acetone, placed in a final spur resin mixture for 3 h, and transferred to final spur resin mixture overnight. They were then placed in 1.5-ml tube contained spur resin, heated at 70 °C for more than 9 h, and sectioned using a LEICA EM UC7 ultratome. Sections were then stained with uranyl acetate and alkaline lead citrate for 5–10 min. Pictures were observed using a transmission electron microscopy (Hitachi, Model H-7650).

2.12. *Mitochondrial morphological analysis*

Cells were stained with 1 μM MitoTracker™ Red FM (Life Technologies, M36008) in RPMI 1640 medium without phenol red (Gibco, 11835030) for 20 min at 37 °C, followed by three washes. Images were captured using a 60 × objective on a confocal microscope (Nikon, A1) with NIS-Elements AR software (Nikon). Resultant images were then analyzed using the Mitochondrial Analyzer plugin in Fiji.

2.13. *Mitochondrial stress analysis*

Real-time oxygen consumption rates (OCR) were measured using the XFe96 extracellular flux analyzer (Seahorse Bioscience). Cells were seeded at 8×10^4 cells per well in XFe96 cell culture microplates (Seahorse Bioscience) and incubated for 5–7 days. OCRs were measured in Seahorse assay medium (10 mM glucose, 10 mM pyruvate, at pH 7.4). Different mitochondrial respiratory states were assessed through the sequential addition of compounds that modulate or inhibit mitochondrial respiration in distinct ways as follows.

First, the ‘basal OCR’ was measured to assess cellular respiration under normal physiological conditions. Then, oligomycin (1.5 μM) was added to determine mitochondrial ‘proton leak’ and ‘ATP-linked OCR’, followed by the addition of the uncoupling agent carbonyl cyanide 4-(trifluoromethoxy)phenylhydrazone (FCCP; 4 μM) to obtain the maximum respiratory rate. The difference between the maximum capacity and basal OCR indicated the ‘reserve capacity’ of the electron transport chain. Finally, a combination of rotenone (0.5 μM) and antimycin A (0.5 μM) was added to inhibit the activity of complexes I and III, respectively, in order to measure non-mitochondrial OCR (NM OCR) and correct for non-mitochondrial sources of OCR.

2.14. *Detection of mitochondrial membrane potential*

For mitochondrial membrane potential detection, cells were stained with Image-iT™ TMRM (Life Technologies, I34361, 1:1000) for 20 min at 37 °C in the dark. After staining, cells were washed three times and examined using a CytoFLEX LX flow cytometer with the mean fluorescence intensity of each sample analyzed using FlowJo.

2.15. *Mitochondrial copy number quantification*

Mitochondrial and genomic DNAs were extracted using a TIANamp Genomic DNA Kit (Tiangen) according to the manufacturer’s instructions. The copy numbers of mitochondrial DNA (mtDNA) and nuclear DNA (nDNA) were quantified using TB Green® Premix Ex Taq™ (Takara) on an ABI Prism 7500 system. Primers specific for ND1, ND5, SLCO2B1, and SERPINA1 were used to quantify mtDNA and nDNA (Takara, 7246), respectively. The difference in the 2ΔCt values for the ND1/SLCO2B1 and ND5/SERPINA1 pairs was determined in the same manner, with the average of the two values used as the mtDNA copy number.

2.16. *Detection of mitochondrial ROS*

For mitochondrial ROS detection, cells were treated with 5 μM MitoSOX (Life Technologies, M36008) at 37 °C for 15 min, followed by three washes. Analysis was conducted using a CytoFLEX LX flow cytometer with the mean fluorescence intensity of each sample analyzed using FlowJo.

2.17. *Cytokine array assay*

Cytokine levels were measured using a Proteome Profiler Human Cytokine Array Kit (Bio-Techne, ARY005B) according to the manufacturer’s instructions. The iPSC-CMs were detached using TrypLE, then pelleted at 1000 rpm for 5 min at 4 °C. All cells were solubilized in lysis buffer at a concentration of 1×10^7 cells/mL. Pipettes were moved up and down to resuspend and agitate the lysates gently at 4 °C for 30 min. The cells were then microcentrifuged at 14,000×*g* for 5 min, and the supernatant was transferred into a clean test tube. Human Cytokine Array Detection Antibody Cocktail was added to each prepared sample. The supernatant was mixed and incubated at room temperature for 1 h, followed by overnight incubated on the membrane. After washing, Streptavidin-HRP was added with incubation for 30 min at room temperature. Membranes were then exposed to an X-ray film for 1–10 min.

2.18. *Real-time quantitative PCR (qPCR)*

Total RNA isolation was performed using TRIzol® Reagent (Life Technologies, 15596018CN). cDNA was obtained using the 4 × EZscript Reverse Transcription Mix II (EZB, EZB-RT2GQ). qPCR was conducted using SYBR Green PCR Master Mix (Takara, RR420A). The mRNA expression values were normalized to *GAPDH*. The sequences of the primers are listed in Supplementary Table 1.

2.19. *Ca^{2+} imaging*

The iPSC-CMs grown on coverslips were loaded with RPMI 1640 medium without phenol red and supplemented with 5 μM Fura-2 AM (Invitrogen, F14185) for 30 min in the dark at room temperature. After washing twice with pre-warmed RPMI 1640, the iPSC-CMs were

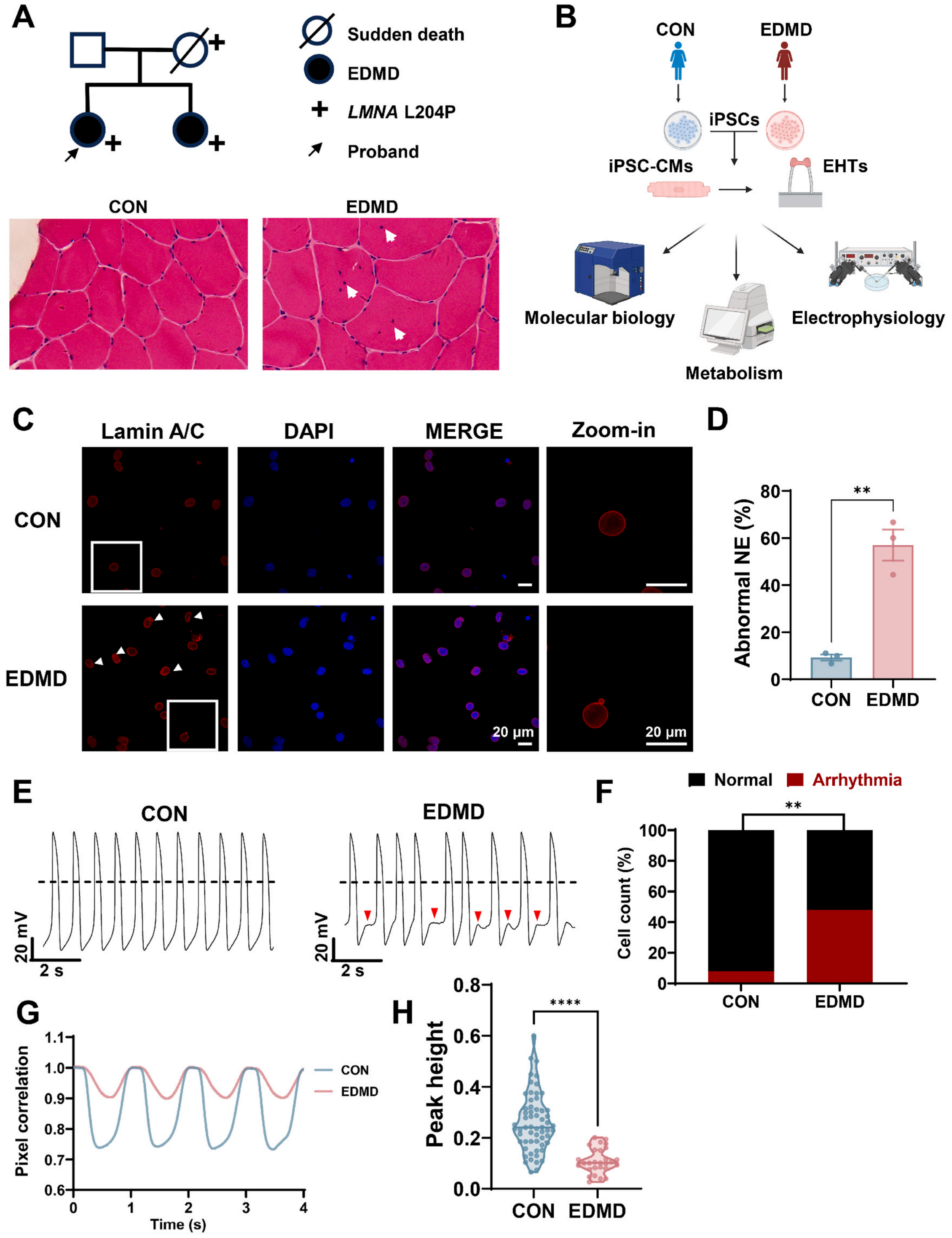

Fig. 1. EDMD patient-specific iPSC-CMs carrying the *LMNA* L204P mutation exhibit arrhythmia and contractile dysfunction. A. Family pedigree (upper), and hematoxylin and eosin (H&E) staining (200 ×) of skeletal muscle tissues from the heathy control subject and the proband (lower). Females are represented by circles, and males by squares. Solid symbols indicate the clinical presentation of the EDMD phenotype, and open symbols represent absence of presentation. "+" signs indicate presence of the *LMNA* L204P mutation. The Arrow indicates the proband. Deceased individuals are marked with a slash. **B.** Schematic diagram of the iPSC lines used in the study. **C.** Representative graphs of staining of lamin A/C (red) in control (CON) and EDMD iPSC-CMs. DAPI indicates nuclear staining (blue). White arrows indicate the abnormal NE. White squares indicate the enlarged area. Scale bar, 20 μm. **D.** Bar graph comparing the percentage of abnormal NE structures between the two groups in C. n = 3 independent experiments. $^{**}p < 0.01$. *p* value was calculated using unpaired two-tailed Student's t-test. Data were shown as mean ± sem. **E.** Representative action potential tracings recorded from CON and EDMD iPSC-CMs by patch clamp. Red arrows indicate arrhythmias. Dash lines indicate 0 mV. **F.** Bar graphs to compare the percentage of cells with arrhythmia between the two groups in E. n = 25 cells. $^{**}p < 0.01$. *p* value was calculated using Fisher's exact test. **G.** Representative contraction tracings recorded from CON and EDMD iPSC-CMs. **H.** Violin graph to compare the peak height of the contraction between the two groups in G. n = 28–60 cells. $^{****}p < 0.0001$. *p* value was calculated using unpaired two-tailed Student's t-test.

immersed in imaging buffer for 30 min prior to imaging experiments. For imaging, iPSC-CMs were placed in a chamber equipped with a temperature controller, under constant perfusion of 37 °C imaging buffer. Ca^{2+} signaling was assessed by recording the fluorescence of cells using an Ultra High Speed Wavelength Switcher (Lambda DG-4, Sutter Instruments) with a CCD camera (Zyla, Andor) mounted on an inverted microscope (Eclipse Ti, Nikon). Fluorescent signals were obtained upon excitation at 340 nm (F_{340}) and 380 nm (F_{380}). The amplitude of a Ca^{2+} transient was defined as the ratio of F_{340}/F_{380}.

2.20. *Detection of calcium content*

The intracellular calcium ion concentration was assessed using a 5 μM Fluo-4 AM Ca^{2+} indicator (Invitrogen, F14201), and mitochondrial calcium concentration was measured using a 5 μM Rhod-2 AM (Invitrogen, R1245MP) Ca^{2+} indicator. Cells were incubated for 15 min at room temperature in the dark. After washing twice with preheated RPMI 1640 medium without phenol red, iPSC-CMs were incubated in imaging buffer for 30 min prior to imaging. Images were captured using a 63 × objective on a Leica TCS SP8 LSCM (Leica Microsystems CMS GmbH, Mannheim, Germany) and analyzed using Fiji.

2.21. *Detection of inflammatory markers in cell culture supernatant*

The concentrations of IL-4, IL-6, IL-10, and IFN-γ in the cell culture supernatant samples were quantitatively measured by flow cytometry. According to the instructions provided by Biotend (XMPlex03240766), the samples were first mixed with a microsphere suspension coated with capture antibodies. The analytes in the samples specifically bound to the capture antibodies on the microspheres. Detection antibodies were then added, binding specifically to the reaction products from the previous step. A fluorophore solution was subsequently added, allowing streptavidin on the fluorophore to bind to the biotin on the detection antibody. Finally, the complex of 'microsphere surface capture antibody-antigen-biotinylated antibody-streptavidin-fluorophore' was formed. Detection was then performed using ABplex-100.

2.22. *Fabrication and culture of human EHTs*

A 1.5 × 8 mm three-dimensional human heart tissue bundle model was made using polydimethylsiloxane (Dow Corning, SYLGARD 184). Each tissue bundle contained approximately 7.5×10^5 iPSC-CMs. Thrombin (Sigma, T7201) was added to the prepared hydrogel solution, which was mixed with Y-27632, Matrigel, fibrinogen (Sigma, F3879), 2 × DMEM (Gibco, 12800017) with horse serum (Solarbio, S9050), Glutamine (Gibco, 25030081), and FBS. The cell/gel mixture was then poured into molds and incubated at 37 °C for 30 min to allow polymerization. Cardiac bundles were removed from the molds and cultured in 12-well plates for 14 days before being used for contractile force testing. The culture medium was refreshed every 2 days.

2.23. *Contractile force assessment of human EHTs*

To assess the force-frequency relationship and electrical-contraction coupling, cardiac bundles were paced with an electrical pulse (10 V, 4 ms) at 1 Hz and 2 Hz using a pair of platinum electrodes in Tyrode's solution containing 1.8 mM Ca^{2+}, and sequentially stretched from 0 % to 20 % of their original length. Data were analyzed using MATLAB software (version R2020b, 9.9.0.1467703).

2.24. *Compounds and solutions*

All the chemicals used in the electrophysiological experiments were purchased from Sigma-Aldrich. Colivelin TFA (CLN) was purchased from MedMol (S20771), and stock solutions were prepared at 50 μg/μl in DMSO.

2.25. *Statistics*

Statistical significance was determined using unpaired two-tailed Student's t-test or Fisher's exact test to compare two groups and by One-way or Two-way ANOVA to compare multiple groups. A p value of <0.05 was considered statistically significant. $^*p < 0.05$, $^{**}p < 0.01$, $^{***}p < 0.001$ and $^{****}p < 0.0001$. Data were shown as mean ± sem and analyzed using GraphPad Prism (GraphPad Software).

2.26. *Data availability*

The accession numbers for the RNA-Seq and ATAC-Seq data reported in this study are PRJNA1229783 and PRJNA1230100, respectively. The data that supports our findings in this study remains available from the corresponding author upon reasonable request.

3. Results

3.1. *Generation of a human-based cardiomyocyte model of LMNA-related EDMD*

To investigate the role of the *LMNA* mutation in EDMD-related cardiac phenotypes, we took advantage of patient-specific iPSCs bearing a heterozygous mutation in the *LMNA* gene (c.611T > C, resulting in p. Leu204Pro, hereafter referred to as L204P) (Fig. 1A and B). These iPSC lines were derived from a 28-year-old female EDMD patient (Supplementary Table 2), who had developed significant cardiac symptoms including palpitations and chest tightness. Electrocardiogram assessment revealed a range of arrhythmias such as sinus bradycardia, sinus arrest, sinoatrial block, and premature ventricular contractions, occurring without any apparent cardiac structural abnormalities. Immunohistochemical analysis of a left bicep muscle biopsy from the proband revealed striking variations in the size and shape of skeletal muscle fibers, sporadic necrosis, and internalized nuclei (Fig. 1A). These findings indicated pathological alterations characteristic of muscular dystrophy. Furthermore, the maternal lineage of this patient was confirmed to include a history of sudden cardiac death (SCD), with the mother having succumbed to cardiac arrest, thus underscoring the significant risk of SCD associated with this *LMNA* mutation (Fig. 1A).

Utilizing the non-integrated Sendai viral method, we successfully generated control (CON) and EDMD patient-specific iPSC lines derived from skin fibroblasts from a healthy donor, and the EDMD patient with the *LMNA* L204P mutation, respectively (Supplementary Table 2). The derived iPSC lines displayed characteristics akin to human embryonic stem cells and exhibiting a similar morphology (Supplementary Fig. 1A). These iPSC lines tested positive for ALP activity (Supplementary Fig. 1A), expressed markers indicative of pluripotency (Supplementary Fig. 1B), and also demonstrated normal karyotypes, (Supplementary Fig. 1C). Sanger sequencing confirmed the presence of the *LMNA* mutation in the EDMD iPSCs (Supplementary Fig. 1D). By employing a small molecule-based monolayer differentiation protocol, both the control and EDMD iPSCs were then directed to differentiate into cardiomyocytes. This method achieved a high efficiency of differentiation, yielding over 95 % purity as confirmed by fluorescence-activated cell sorting (FACS) analysis (Supplementary Figs. 2A–C). The protein levels of lamin A/C, the products of the *LMNA* gene, were then assessed using Western blot, showing significantly diminished in EDMD iPSC-CMs compared to controls (Supplementary Figs. 2D and E). The morphology of the sarcomeres and NE was detected via immunofluorescence. Interestingly, EDMD iPSC-CMs presented with a significantly higher proportion of disorganized NE structures and obvious signs of nuclear blebbing (CON: 9.27 ± 2.29 %; EDMD: 57.03 ± 11.44 %) (Fig. 1C, D and Supplementary Fig. 2F). Collectively, we concluded the successful establishment of a robust human-based *in vitro* model to study cardiac manifestations linked to the *LMNA* mutation in EDMD.

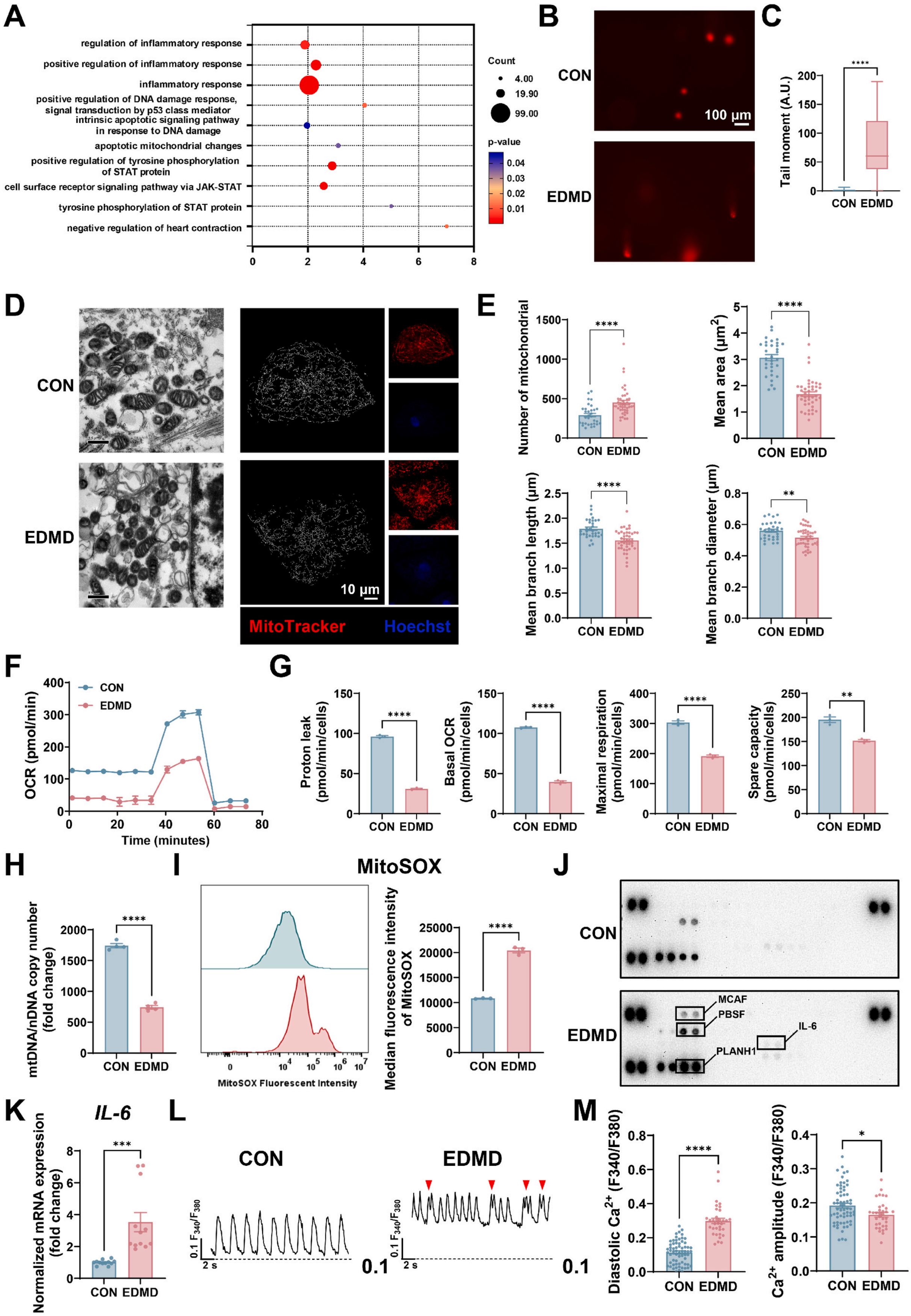

(caption on next page)

Fig. 2. Pathogenic signature of mitochondrial dysfunction and inflammatory activation in EDMD iPSC-CMs. A. GO analysis identified significant changes in inflammation, mitochondrial function, muscle contraction, and DNA damage. **B.** Representative graphs of DNA damage in CON and EDMD iPSC-CMs, as measured by comet assay. Scale bar, 100 μm. **C.** Box & whiskers graph to compare the tail moment between CON and EDMD iPSC-CMs. n = 60–63 cells. A.U., arbitrary units. $****p < 0.0001$. *p* value was calculated using unpaired two-tailed Student's t-test. Whiskers were shown as min to max. **D.** Representative graphs of mitochondria in CON and EDMD iPSC-CMs by transmission electron microscopy and staining of MitoTracker (Red). Hoechst indicates nuclear staining (blue). Scale bar, 10 μm. **E.** Bar graphs to compare the mitochondrial-related parameters (number of mitochondrial, mean area, mean branch length, mean branch diameter) between the two groups in D. n = 32–43 cells. $**p < 0.01$ and $****p < 0.0001$. *p* values were calculated using unpaired two-tailed Student's t-test. Data were shown as mean ± sem. **F.** Analysis of oxygen consumption in CON and EDMD iPSC-CMs. n = 3 independently biological repeats. **G.** Bar graphs to compare key parameters of OCR between the two groups in F. n = 3 independently biological repeats. $**p < 0.01$ and $****p < 0.0001$. *p* values were calculated using unpaired two-tailed Student's t-test. Data were shown as mean ± sem. **H.** Bar graph to compare the mitochondrial DNA (mtDNA)/nuclear DNA (nDNA) ratio between CON and EDMD iPSC-CMs. n = 4 independently biological repeats. $****p < 0.0001$. *p* value was calculated using unpaired two-tailed Student's t-test. Data were shown as mean ± sem. **I.** Mitochondrial ROS levels in CON and EDMD iPSC-CMs. n = 3 independently biological repeats. $****p < 0.0001$. *p* value was calculated using unpaired two-tailed Student's t-test. Data were shown as mean ± sem. **J.** Representative graphs of dot blot in CON and EDMD iPSC-CMs. The black box marks the increase in EDMD iPSC-CMs. **K.** Bar graph to compare the mRNA expression of JAK2 between CON and EDMD iPSC-CMs. n = 12 independently biological repeats. $***p < 0.001$. *p* value was calculated using unpaired two-tailed Student's t-test. Data were shown as mean ± sem. **L,** Representative Ca^{2+} transient traces recorded from CON and EDMD iPSC-CMs. **M.** Bar graphs to compare the diastolic Ca^{2+} and Ca^{2+} transient amplitude between the two groups in L. n = 34–64 cells. $*p < 0.05$ and $****p < 0.0001$. *p* values were calculated using unpaired two-tailed Student's t-test. Data were shown as mean ± sem.

3.2. *Arrhythmogenic traits and contractile dysfunction in EDMD iPSC-CMs*

Given the pronounced cardiac symptoms and the heightened risk of SCD linked to this mutation, we initiated our investigation by examining the electrophysiological characteristics of EDMD iPSC-CMs. This was accomplished by recording single-cell action potentials from control and EDMD iPSC-CMs to gain insight into their potential arrhythmogenic properties. We observed a uniform and rhythmic action potential profile in control iPSC-CMs (Fig. 1E and F). By contrast, arrhythmic waveforms were detected in a large proportion of EDMD iPSC-CMs (CON: 8 %; EDMD: 48 %). As myocardial contractility serves as a pivotal parameter for assessing cardiac function, we proceeded to evaluate the contractile force of EDMD iPSC-CMs utilizing the IonOptix system. The peak amplitude of contraction in EDMD iPSC-CMs was revealed as significantly reduced compared to that observed in control iPSC-CMs (CON: 0.26 ± 0.11; EDMD: 0.11 ± 0.05) (Fig. 1G and H). Taken together, these results demonstrate arrhythmogenic traits and contractile dysfunction in EDMD iPSC-CMs.

3.3. *EDMD iPSC-CMs exhibit a pathological profile of mitochondrial dysfunction and inflammatory activation*

To elucidate the impact of the *LMNA* mutation upon EDMD at the transcriptome level, we conducted RNA-Seq on both control and EDMD iPSC-CMs. GO enrichment analysis revealed that differentially expressed genes were primarily linked to inflammation, mitochondrial function, and DNA damage (Fig. 2A). To evaluate the level of DNA damage, we performed a comet assay in control and EDMD iPSC-CMs (Fig. 2B and C). EDMD iPSC-CMs exhibited a significantly higher distribution in the percentage of DNA found in the comet tail (CON: 0.41 ± 1.03; EDMD: 72.85 ± 53.58) (Fig. 2C). We next assessed the expression levels of phosphorylated Histone H2A.X (p-Histone H2A.X) using Western blot and immunofluorescence. These analyses revealed a markedly elevated level of p-Histone H2A.X in EDMD iPSC-CMs as compared to control counterparts (Supplementary Figs. 3A–D). These results indicated the existence of DNA damage in EDMD iPSC-CMs. We then examined mitochondrial morphology via transmission electron microscopy. This revealed mitochondrial fragmentation in EDMD iPSC-CMs (Fig. 2D and E). To assess mitochondrial respiratory function, we quantified the OCR of iPSC-CMs using a Seahorse bioscience XF-96 extracellular flux analyzer. Parameters of proton leak, basal OCR, maximal capacity, and spare capacity were all significantly diminished in EDMD iPSC-CMs, compared to controls (Fig. 2F and G). Meanwhile, we assessed the mitochondrial membrane potential using flow cytometry combined with a fluorescent TMRM probe. We observed that the mitochondrial membrane potential levels were significantly lower in EDMD iPSC-CMs than that in controls (Supplementary Fig. 3E). Additionally, the mitochondrial DNA (mtDNA) copy number was found to be significantly reduced in EDMD iPSC-CMs (Fig. 2H). Altogether, these results indicate significantly compromised mitochondrial bioenergetics in EDMD iPSC-CMs.

Given the correlation between mitochondrial dysfunction and heightened ROS generation, and recognizing that mitochondria are a primary source of ROS [37,38], we proceeded to evaluate mitochondrial ROS production using flow cytometry with the aid of the fluorescent probe MitoSOX. The level of mitochondrial ROS was significantly higher in EDMD iPSC-CMs than that in controls (Fig. 2I). Considering the pronounced enrichment of inflammatory pathways in our RNA-Seq data, we then examined the level of inflammatory factors in EDMD iPSC-CMs. This revealed a significantly upregulated level of IL-6 in comparison with control iPSC-CMs (Fig. 2J). qPCR results also revealed significantly higher mRNA levels of *IL-6* in EDMD iPSC-CMs than that in controls (Fig. 2K). Previous studies have provided increasing evidence pointing to a reciprocal interaction between Ca^{2+} and ROS signaling pathways, indicating crucial roles for this in the regulation of cellular signaling networks [39,40]. We therefore assessed Ca^{2+} transients from control and EDMD iPSC-CMs by Fura-2 Ca^{2+} imaging (Fig. 2L). The Ca^{2+} transient amplitude was significantly lower in EDMD iPSC-CMs (CON: 0.19 ± 0.06; EDMD: 0.17 ± 0.04) (Fig. 2M) than in controls. Moreover, we observed significantly increased diastolic intracellular Ca^{2+} ($[Ca^{2+}]_i$) in EDMD iPSC-CMs (CON: 0.11 ± 0.07; EDMD: 0.30 ± 0.09) (Fig. 2M). The Ca^{2+} load of mitochondria, as detected by rhod2 staining, was also revealed as having a higher Ca^{2+} load in EDMD iPSC-CMs (Supplementary Fig. 3F). Perturbed Ca^{2+} homeostasis may therefore underlie the cardiac pathogenic phenotypes observed in EDMD iPSC-CMs. Taken together, these results demonstrate a pathogenic signature of mitochondrial dysfunction, inflammatory activation, and abnormal Ca^{2+} signaling, in EDMD iPSC-CMs.

3.4. *The JAK2/STAT3 signaling pathway is suppressed in EDMD iPSC-CMs*

As the *LMNA* mutations had resulted in reduced nuclear stability and deformation of the nuclear envelop in skeletal muscle cells [8], we therefore considered that the *LMNA* L204P mutation act to alter chromatin accessibility and cause changes in the gene transcription level in EDMD iPSC-CMs. Through the comprehensive analysis of RNA-Seq and ATAC-Seq for control and EDMD iPSC-CMs, we identified a particular gene of interest, namely *JAK2* (Fig. 2A and Supplementary Fig. 4). In spite of inflammatory activation, the expression of *JAK2* was downregulated in RNA-Seq (Supplementary Fig. 4A) in EDMD iPSC-CMs, a factor also confirmed by qPCR and Western blot (Supplementary Fig. 2D and E and 4B). GO analysis similarly identified significant mutational effects upon JAK2-related pathways (Fig. 2A). By conducting a thorough analysis of ATAC-Seq data, we confirmed a reduction in chromatin

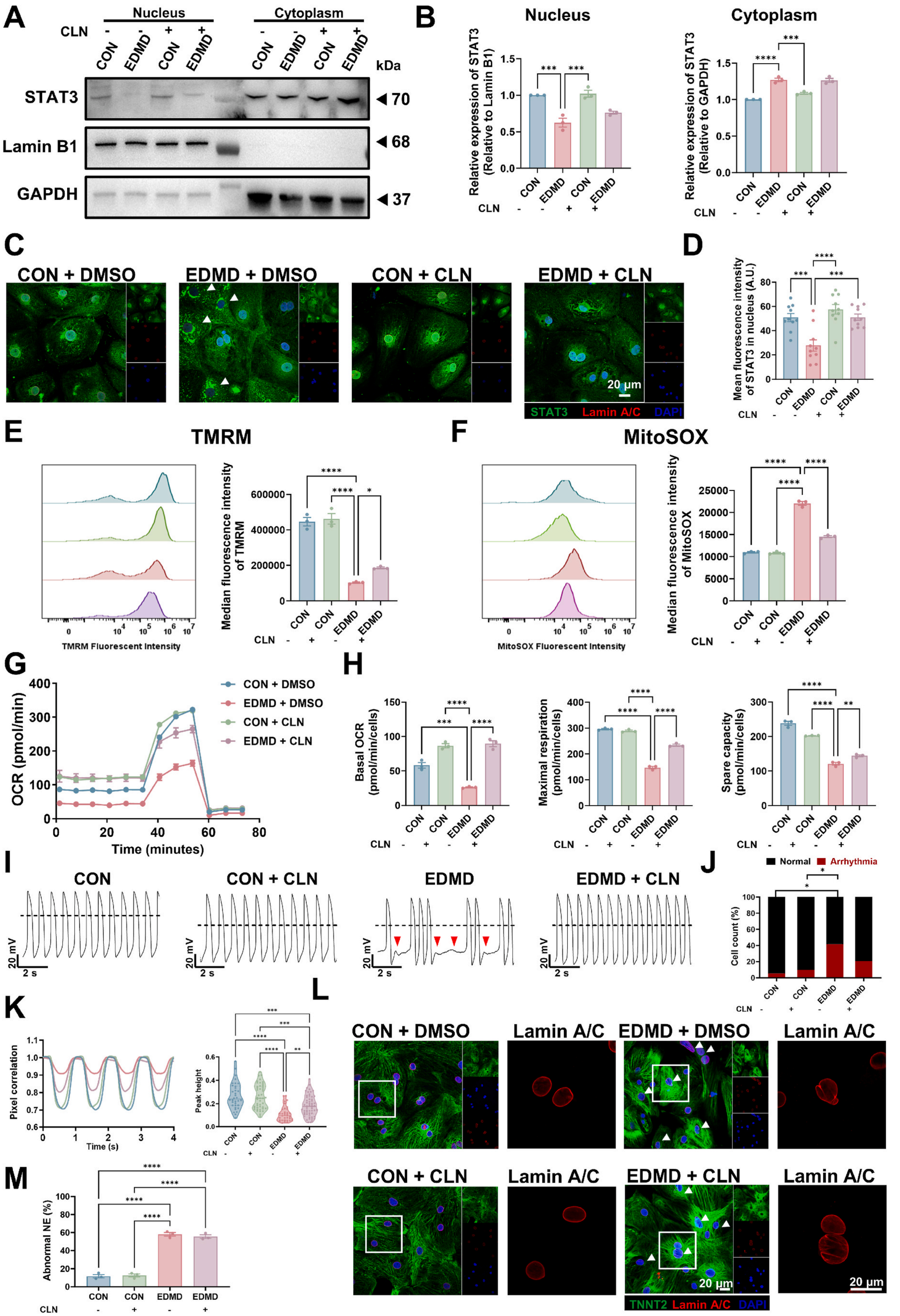

(caption on next page)

Fig. 3. Pharmacological activation of JAK2/STAT3 signaling rescues the arrhythmic and contractile dysfunction phenotypes of EDMD iPSC-CMs by improving mitochondrial function. A. Western blot analysis of the protein expression of cytosol and nuclear STAT3 in CON and EDMD iPSC-CMs with or without Colivelin (CLN) treatment. **B.** Bar graph to compare the protein expression in A. 3 independently biological repeats. ***$p < 0.001$ and ****$p < 0.0001$. p values were calculated using One-way ANOVA. Data were shown as mean ± sem. **C.** Representative graphs of co-staining of lamin A/C (red) and STAT3 (green) in CON and EDMD iPSC-CMs with or without CLN treatment. DAPI indicates nuclear staining (blue). White arrows indicate cells without the nuclear localization of STAT3. Scale bar, 20 μm. **D.** Bar graph to compare the mean fluorescence intensity of STAT3 in nucleus among different groups in C. $n = 10$ independently biological repeats. ***$p < 0.001$ and ****$p < 0.0001$. p values were calculated using One-way ANOVA. Data were shown as mean ± sem. **E.** TMRM levels in CON and EDMD iPSC-CMs with or without CLN treatment. $n = 3$ independently biological repeats. *$p < 0.05$ and ****$p < 0.0001$. p values were calculated using One-way ANOVA. Data were shown as mean ± sem. **F.** Mitochondrial ROS levels in CON and EDMD iPSC-CMs with or without CLN treatment. $n = 3$ independently biological repeats. ****$p < 0.0001$. p values were calculated using One-way ANOVA. Data were shown as mean ± sem. **G.** Analysis of oxygen consumption in CON and EDMD iPSC-CMs with or without treatment of CLN. $n = 3$ independently biological repeats. **H.** Bar graphs to compare key parameters of OCR among different groups in G. $n = 3$ independently biological repeats. **$p < 0.01$, ***$p < 0.001$ and ****$p < 0.0001$. p values were calculated using One-way ANOVA. Data were shown as mean ± sem. **I.** Representative action potential tracings recorded from CON and EDMD iPSC-CMs with or without CLN by patch clamp. Red arrows indicate arrhythmias. Dash lines indicate 0 mV. **J.** Bar graph to compare the percentage of cells with arrhythmia among different groups in H. $n = 18–34$ cells. *$p < 0.05$. p values were calculated using Fisher's exact test. **K.** Representative contraction tracings recorded from CON and EDMD iPSC-CMs with or without CLN. Violin graph to compare the peak height of the contraction among different groups. $n = 34–56$ cells. **$p < 0.01$, ***$p < 0.001$ and ****$p < 0.0001$. p values were calculated using One-way ANOVA. **L.** Representative graphs of staining of lamin A/C (red) in CON and EDMD iPSC-CMs with or without CLN treatment. DAPI indicates nuclear staining (blue). White arrows indicate abnormal NE. White squares indicate the enlarged area. Scale bar, 20 μm. **M.** Bar graph to compare the percentage of abnormal NE structure among different groups in L. $n = 3$ independent experiments. ****$p < 0.0001$. p values were calculated using One-way ANOVA. Data were shown as mean ± sem.

accessibility at the *JAK2* locus, accounting for the anomalous downregulation of *JAK2* (Supplementary Figs. 4C and D).

Our previous investigations had revealed impaired mitochondrial function in EDMD iPSC-CMs, leading to excessive ROS production. Given the pivotal role of JAK2/STAT3 in mitochondrial function [24,28,31,32], we next assessed the expression levels of JAK2 and STAT3 in control and EDMD iPSC-CMs. We observed a significant reduction in the levels of JAK2 and phosphorylated STAT3 (at residues 705 and 727) in EDMD iPSC-CMs, while no significant change of total STAT3 was observed between control and EDMD iPSC-CMs (Supplementary Figs. 5A–C). Immunofluorescence analysis further revealed a marked reduction in the nuclear distribution of STAT3 in EDMD iPSC-CMs, when compare to controls (Supplementary Figs. 5D and E). Moreover, the mRNA levels of downstream genes of STAT3 were significantly downregulated in EDMD iPSC-CMs (Supplementary Fig. 5F). These results suggest that the JAK2/STAT3 signaling pathway is suppressed in EDMD iPSC-CMs, a factor which may contribute to the cardiac phenotypes of EDMD.

3.5. *Pharmacological activation of JAK2/STAT3 signaling rescues the arrhythmic and contractile dysfunction phenotypes of EDMD iPSC-CMs by improving mitochondrial function*

To link suppressed JAK2/STAT3 and the pathogenic phenotypes observed in EDMD iPSC-CMs, pharmacological activation of JAK2/STAT3 was applied in EDMD iPSC-CMs. Treatment of CLN, a potent activator of STAT3, significantly increased the distribution of STAT3 in the nuclei of EDMD iPSC-CMs, in clear contrast to cells receiving the DMSO (vehicle) treatment (Fig. 3A–D). The levels of mitochondrial membrane potential and mitochondrial ROS were similarly significantly improved in CLN group compared to DMSO group (Fig. 3E and F). Mitochondrial function was also rescued in the CLN group, with the parameters of basal OCR, maximal capacity, and spare capacity all significantly elevated (Fig. 3G and H). Notably, the arrhythmic phenotype (CON + DMSO: 5.60 %; CON + CLN: 9.50 %; EDMD + DMSO: 41.70 %; EDMD + CLN: 20.60 %) and compromised contractile function (CON + DMSO: 0.27 ± 0.11; CON + CLN: 0.26 ± 0.11; EDMD + DMSO: 0.11 ± 0.07; EDMD + CLN: 0.18 ± 0.09) in EDMD iPSC-CMs were substantially rescued by CLN treatment (Fig. 3I–K), suggesting the pivotal role of the JAK2/STAT3 signaling pathway in the pathogenesis of EDMD. Furthermore, treatment of Mito-TEMPO, the mitochondrial ROS scavenger, significantly eliminated the mitochondrial ROS production (Supplementary Fig. 6A) and ameliorated key pathogenic phenotypes observed in EDMD iPSC-CMs. Specifically, this intervention markedly reduced arrhythmic events (Supplementary Figs. 6B and C), improved contractile function (Supplementary Fig. 6D), downregulated pro-inflammatory cytokines (Supplementary Fig. 6E), and alleviated Ca^{2+} abnormalities (Supplementary Fig. 6F). However, neither CLN nor Mito-TEMPO had no significant rescue effect on the abnormal NE structure phenotype in EDMD iPSC-CMs (Fig. 3L–M and Supplementary Figs. 6G–H), suggesting that the molecular mechanisms underlying functional abnormalities and NE structural abnormality may be independent. Altogether, these results suggest that activation of JAK2/STAT3 signaling pathway is able to rescue the arrhythmic and contractile dysfunction phenotypes of EDMD iPSC-CMs by improving mitochondrial function.

3.6. *Genetic inhibition of JAK2 in control iPSC-CMs recapitulates the arrhythmic and contractile dysfunction phenotypes of EDMD iPSC-CMs*

The suppressed JAK2/STAT3 signaling pathway in EDMD iPSC-CMs appears to result in mitochondrial dysfunction and overproduction of ROS. This could be the underlying cause of the observed arrhythmic phenotype and contractile impairment. To establish a direct link between JAK2 and these pathogenic phenotypes, we employed small interfering RNA (siRNA) to genetically suppress JAK2 expression in control iPSC-CMs. The efficiency of JAK2 knockdown (KD) was confirmed through Western blot analysis, which revealed a significant reduction in the levels of JAK2, phosphorylated STAT3 at residues 705 and 727, and phosphorylated DRP1 (an essential element in the maintenance of both mitochondrial fission and mitochondrial homeostasis) (Fig. 4A and B) [41]. Moreover, the JAK2 siRNA-treated control iPSC-CMs displayed a marked decline in mitochondrial function compared to those treated with scrambled siRNA (negative control, NC), with maximal capacity and spare capacity both being significantly reduced (Fig. 4C and D). In parallel, control iPSC-CMs with JAK2 KD exhibited phenotypic traits indicative of the related pathologies, including arrhythmias (CON-NC: 11.10 %; CON-KD: 26.30 %) and contractile dysfunction (CON-NC: 0.26 ± 0.13; CON-KD: 0.14 ± 0.07) (Fig. 4E–G). Collectively, these results suggest that the genetic inhibition of JAK2 in control iPSC-CMs can recapitulate the arrhythmic and contractile dysfunction phenotypes of EDMD iPSC-CMs.

3.7. *Overexpression of JAK2 rescues the arrhythmic and contractile dysfunction phenotypes of EDMD iPSC-CMs by alleviating mitochondrial dysfunction*

Having shown that the pharmacological activation of JAK2/STAT3 can ameliorate the arrhythmic and contractile dysfunction phenotypes of EDMD iPSC-CMs, and that genetic inhibition of JAK2 results in recapitulation of these EDMD cardiomyocyte phenotypes in control iPSC-CMs, we then constructed a human wild-type (WT) JAK2 plasmid with GFP tag in order to further confirm the causal relationship between JAK2 and these pathogenic phenotypes. In this, GFP only (negative

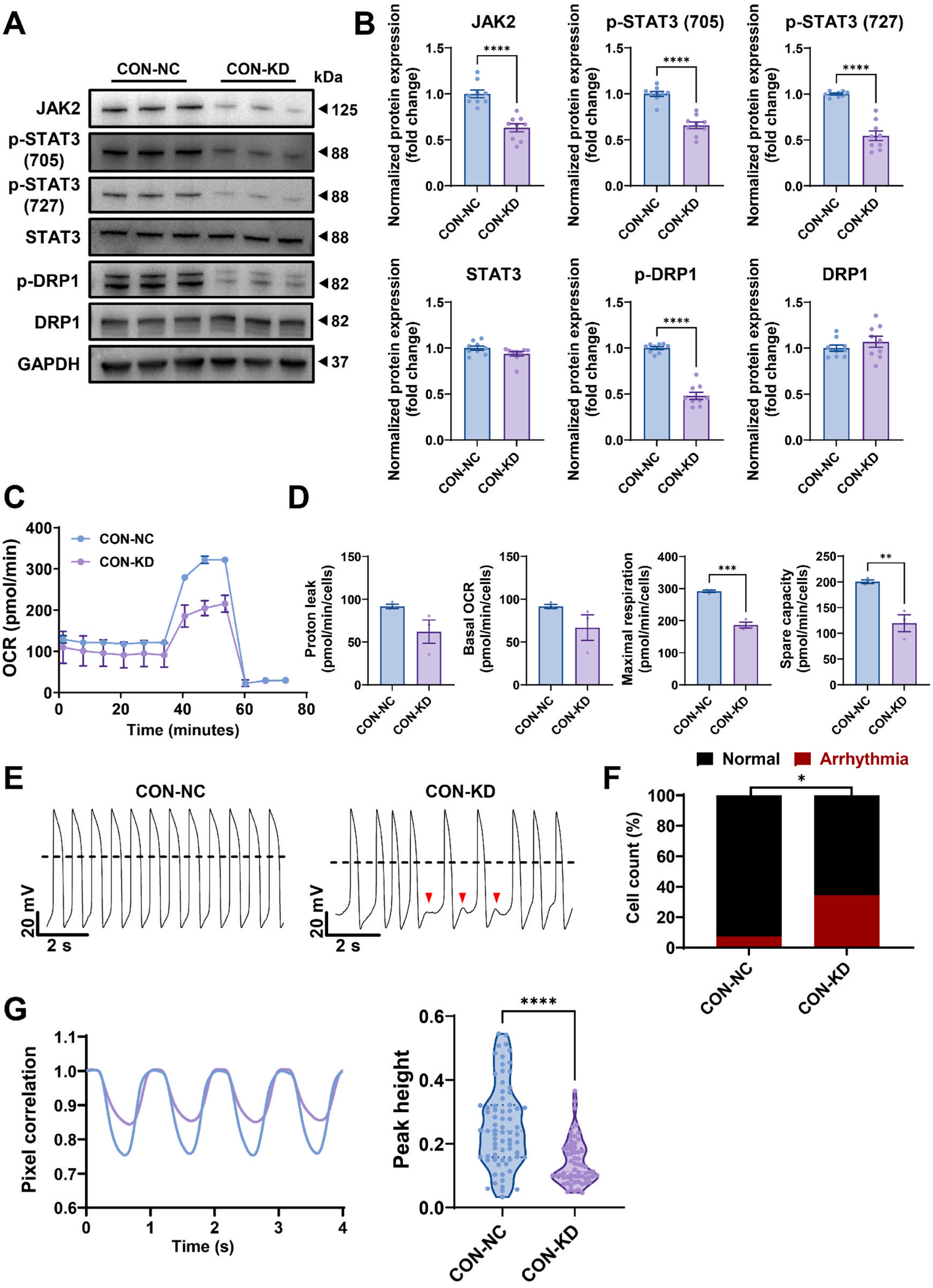

Fig. 4. Genetic inhibition of JAK2 in control iPSC-CMs recapitulates the arrhythmic and contractile dysfunction phenotypes of EDMD iPSC-CMs. A. Western blot analysis of JAK2, p-STAT3 (727 and 705), STAT3, *p*-DRP1, and DPR1 expression in CON iPSC-CMs treated with scrambled siRNA (negative control, NC) or JAK2 siRNA (knockdown, KD). **B.** Bar graphs to compare the protein expression between CON-NC and CON-JAK2-KD iPSC-CMs in A. n = 9 independently biological repeats. $****p < 0.0001$. *p* values were calculated using unpaired two-tailed Student's t-test. Data were shown as mean ± sem. **C.** Analysis of oxygen consumption in CON-NC and CON-JAK2-KD iPSC-CMs. n = 3 independently biological repeats. **D.** Bar graphs to compare key parameters of OCR between different groups in C. n = 3 independently biological repeats. $**p < 0.01$ and $***p < 0.001$. *p* values were calculated using unpaired two-tailed Student's t-test. Data were shown as mean ± sem. **E.** Representative action potential tracings recorded from CON-NC and CON-JAK2-KD iPSC-CMs by patch clamp. Red arrows indicate arrhythmias. Dash lines indicate 0 mV. **F.** Bar graph to compare the percentage of cells with arrhythmia between the two groups in E. n = 27–29 cells. $*p < 0.05$. *p* value was calculated using Fisher's exact test. **G.** Representative contraction tracings recorded from CON-NC and CON-JAK2-KD iPSC-CMs. Violin graph to compare the peak height of the contraction between the two groups. n = 63–71 cells. $****p < 0.0001$. *p* value was calculated using unpaired two-tailed Student's t-test.

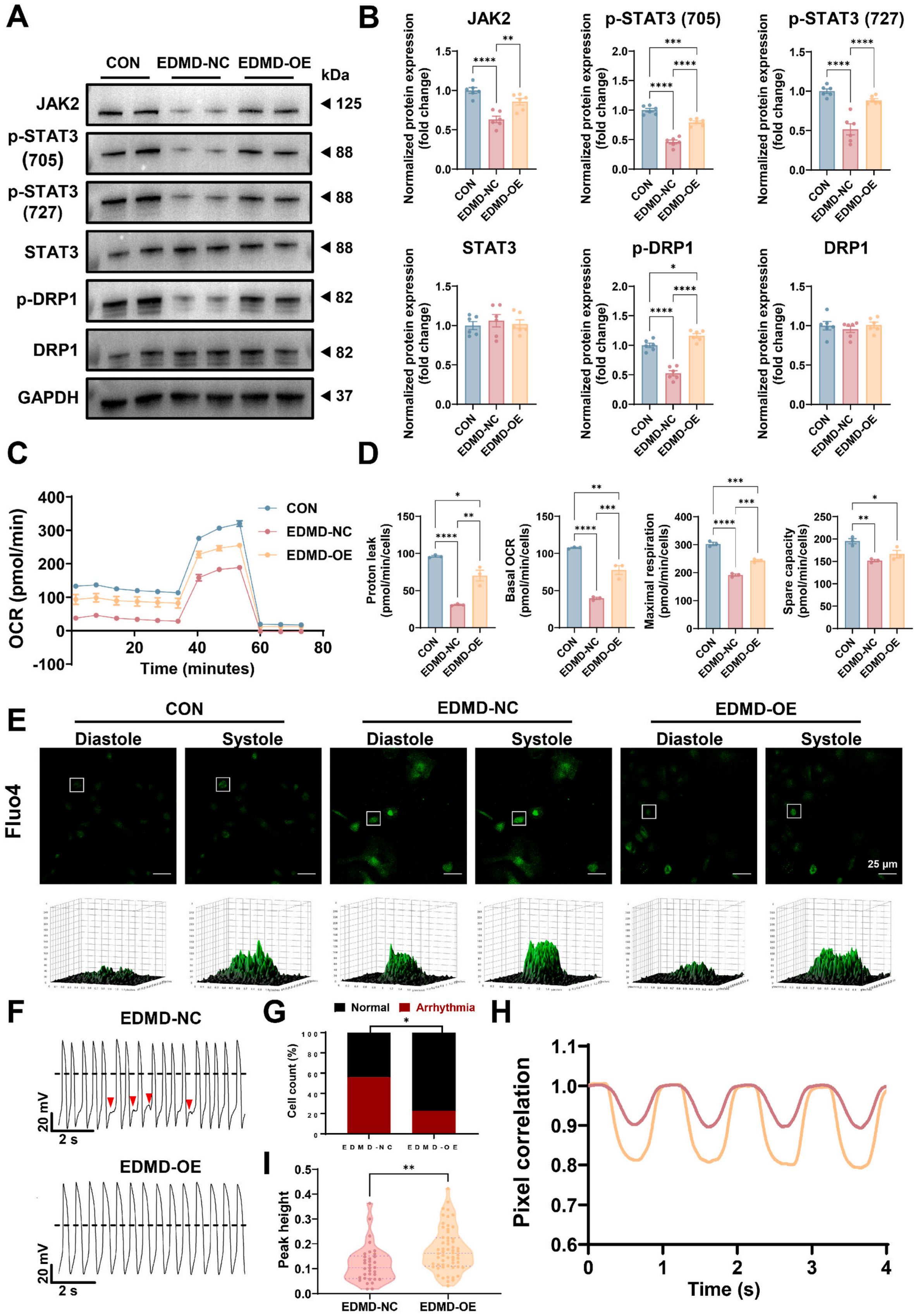

(caption on next page)

Fig. 5. Overexpression of JAK2 rescues the arrhythmic and contractile dysfunction phenotypes of EDMD iPSC-CMs by alleviating mitochondrial dysfunction. A. Western blot analysis of JAK2, p-STAT3 (727 and 705), STAT3, *p*-DRP1, and DPR1 expression in CON, EDMD-NC and EDMD-JAK2-OE iPSC-CMs. **B.** Bar graphs to compare the protein expression in A. n = 6 independently biological repeats. $^*p < 0.05$, $^{**}p < 0.01$, $^{***}p < 0.001$ and $^{****}p < 0.0001$. *p* values were calculated by One-way ANOVA. Data were shown as mean ± sem. **C.** Analysis of oxygen consumption in CON, EDMD-NC and EDMD-JAK2-OE iPSC-CMs. n = 3 independently biological repeats. **D.** Bar graphs to compare key parameters of OCR among different groups in C. n = 3 independently biological repeats. $^*p < 0.05$, $^{**}p < 0.01$, $^{***}p < 0.001$ and $^{****}p < 0.0001$. *p* values were calculated by One-way ANOVA. Data were shown as mean ± sem. **E.** Representative graphs of staining of Fluo4 in CON, EDMD-NC and EDMD-JAK2-OE iPSC-CMs during diastole or systole. Each graph below shows the corresponding 3D surface plot. Scale bar, 25 μm. **F.** Representative action potential tracings recorded from EDMD-NC and EDMD-JAK2-OE iPSC-CMs by patch clamp. Red arrows indicate arrhythmias. Dash lines indicate 0 mV. **G.** Bar graph to compare the percentage of cells with arrhythmia between the two groups in F. n = 22–25 cells. $^*p < 0.05$. *p* value was calculated using Fisher's exact test. **H.** Representative contraction tracings recorded from EDMD-NC and EDMD-JAK2-OE iPSC-CMs. **I.** Violin graph to compare the peak height of the contraction between the two groups. n = 34–58 cells. $^{**}p < 0.01$. *p* value was calculated using unpaired two-tailed Student's t-test.

control, NC) or JAK2-GFP was successfully transfected into EDMD iPSC-CMs. The overexpression (OE) of JAK2 in EDMD iPSC-CMs led to a pronounced increase in JAK2 protein expression, accompanied by significant elevation in the phosphorylation of STAT3 (at residues 705 and 727) and DRP1 (Fig. 5A and B). In turn, this resulted in the morphological and functional integrity of mitochondria in EDMD iPSC-CMs being notably restored by JAK2 OE (Supplementary Figs. 7A and B). JAK2 OE in EDMD iPSC-CMs also led to significantly decreased mitochondrial ROS and inflammatory levels, and increased mtDNA copy number (Supplementary Figs. 7C–E). Moreover, the mitochondrial function was effectively rescued in EDMD iPSC-CMs after JAK2 OE, where the parameters of proton leak, basal OCR, maximal capacity, and spare capacity were all significantly elevated (Fig. 5C and D). The aberrant Ca^{2+} handling characteristic of EDMD iPSC-CMs was also significantly improved by JAK2 OE, as indicated by enhanced Ca^{2+} transient amplitude, reduced diastolic Ca^{2+} level, and reduced mitochondrial Ca^{2+} load (Fig. 5E and Supplementary Fig. 7F). Notably, the arrhythmic phenotype (EDMD-NC: 56.00 %; EDMD-OE: 27.30 %) and compromised contractile function (EDMD-NC: 0.12 ± 0.08; EDMD-OE: 0.18 ± 0.09) in EDMD iPSC-CMs were substantially rescued by JAK2 OE (Fig. 5F–I). Taken together, the overexpression of JAK2 can rescue the arrhythmic and contractile dysfunction phenotypes in EDMD iPSC-CMs by alleviating the associated mitochondrial dysfunction.

3.8. *Rescuing the arrhythmic and contractile dysfunction phenotypes of EDMD iPSC-CMs by genetic correction of the LMNA P204P mutation*

To eliminate the potential confounding effects of genetic background, we successfully generated a gene-corrected (GC) isogenic iPSC line by correcting the *LMNA* L204P mutation in EDMD iPSCs (Supplementary Figs. 8A–E). Patch clamp recordings revealed a dramatic reduction of arrhythmic incidences in GC iPSC-CMs, representing action potentials restored to levels comparable to those from controls (CON: 6.3 %; GC: 7.9 %; EDMD: 39.1 %) (Fig. 6A and B). IonOptix assays also revealed a significantly higher peak amplitudes of contraction in GC iPSC-CMs than that in EDMD iPSC-CMs (CON: 0.29 ± 0.14; GC: 0.28 ± 0.14; EDMD: 0.21 ± 0.11) (Fig. 6C and D). Moreover, the level of mitochondrial ROS was significantly reduced in GC iPSC-CMs as compared to EDMD iPSC-CMs (Fig. 6E). Western blot and immunofluorescence analyses revealed the significantly increased expression of lamin A, lamin C, JAK2, and phosphorylated STAT3 and DRP1, along with significantly increased nuclear localization of STAT3 in GC iPSC-CMs, when compared to EDMD iPSC-CMs (Fig. 6F–I and Supplementary Figs. 8F and G). Mitochondrial fragmentation was also significantly alleviated in GC iPSC-CMs as compared to EDMD iPSC-CMs (Fig. 6J and K). The resultant GC iPSC-CMs exhibited a restored profile resembling that of control iPSC-CMs. Taken together, these results demonstrate that genetic correction of the *LMNA* L204P mutation is sufficient to rescue the arrhythmic and contractile dysfunction phenotypes of EDMD iPSC-CMs.

3.9. *The JAK2/STAT3 signaling pathway is suppressed in EDMD iPSC-derived skeletal muscle cells*

To investigate molecular alterations in the JAK2/STAT3 pathway within skeletal muscle pathology, we established an *in vitro* model through the differentiation of iPSCs into skeletal muscle cells (iPSC-SMCs). Immunofluorescence analysis revealed a marked reduction in myotube formation capacity in EDMD iPSC-SMCs compared to controls (Supplementary Figs. 9A and B). Subsequent quantification of myogenic differentiation markers demonstrated significantly decreased mRNA expression levels of *MYOD*, *MYOG* and *MYHC* in EDMD iPSC-SMCs on day 16 post-differentiation (Supplementary Fig. 9C). These results suggest impaired differentiation progression occurring from myoblasts, through to myocytes, and on to mature myotubes. According to previous findings in the iPSC-CMs, we performed pathway validation in iPSC-SMCs. qPCR analysis showed significantly reduced *JAK2* mRNA expression in EDMD iPSC-SMCs (Supplementary Fig. 9D), while *STAT3* levels remained comparable between control and EDMD iPSC-SMCs (Supplementary Fig. 9E). Meanwhile, qPCR analysis identified significantly higher level of *IL-6* (Supplementary Fig. 9F), and downregulation of STAT3-downstream target genes (Supplementary Fig. 9G). These findings suggest that EDMD iPSC-SMCs exhibit a suppressed JAK2/STAT3 signaling pathway similar to those observed in iPSC-CMs.

3.10. *Pharmacological activation of JAK2/STAT3 signaling improves the function of EDMD patient-specific EHTs*

To further assess the therapeutic impact of STAT3 activation at the tissue level, we then developed a human EHT model. At baseline, EDMD EHTs exhibited a noncompacted morphology, in contrast to the compacted appearance of control and GC EHTs (Fig. 7A). Contraction waveforms were captured for control, GC, and EDMD EHTs under incremental stretch lengths (stretching ratio: 0–8 %) at a frequency of 2 Hz. The contractile force of EDMD EHTs was markedly reduced at 0 %, 4 % and 8 % stretching ratios, as conducted at a 2 Hz pacing frequency, compared to control and GC EHTs (Fig. 7B). After treatment with CLN for a duration of 4 h, the impairment of contraction was notably mitigated in EDMD iPSC-CMs as compared to controls (Fig. 7C). These findings indicate that EDMD EHTs accurately reflect the same pathological contractile dysfunction phenotype, which can then be substantially ameliorated by STAT3 activation.

4. Discussion

In this study, we employed patient-specific and genome-edited iPSC-CM and EHT models to investigate the underlying mechanisms of pathogenic cardiac phenotypes in *LMNA*-related EDMD. EDMD iPSC-CMs carrying the *LMNA* L204P mutation were observed to exhibit the classic pathogenic phenotypes of arrhythmia and contractile dysfunction. L204P iPSC-CMs also displayed DNA damage, disruptions in mitochondrial homeostasis, and inflammatory activation. These observed abnormalities were attributed to the restricted activity of the JAK2/STAT3 signaling pathway. Combined RNA-Seq and ATAC-Seq analysis revealed that *LMNA* L204P resulted in decreased chromatin

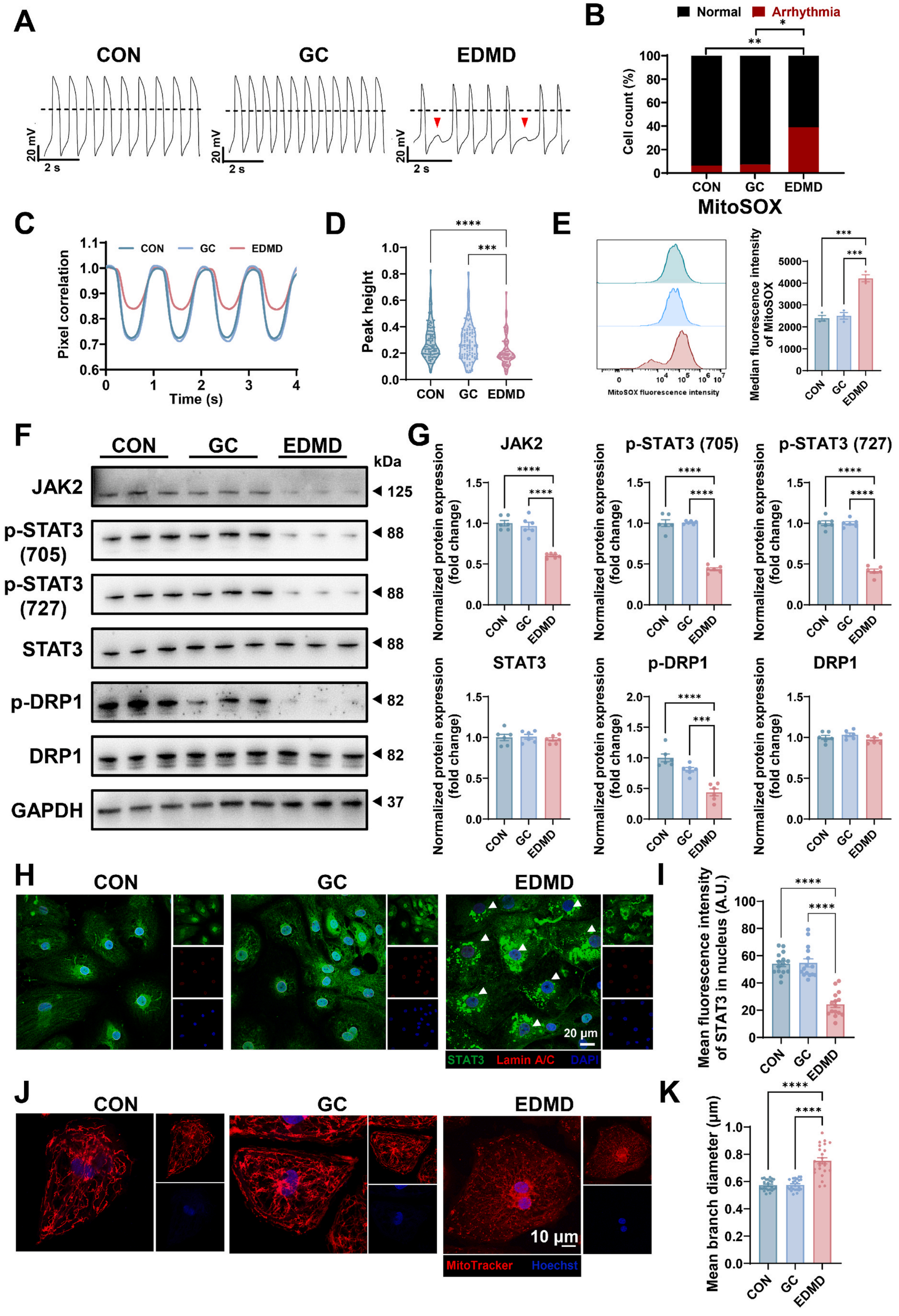

(caption on next page)

Fig. 6. Rescuing the arrhythmic and contractile dysfunction phenotypes of EDMD iPSC-CMs by genetic correction of the *LMNA* P204P mutation. A. Representative action potential tracings recorded from CON, GC and EDMD iPSC-CMs by patch clamp. Red arrows indicate arrhythmias. Dash lines indicate 0 mV. **B.** Bar graph to compare the percentage of cells with arrhythmia among different groups in A. n = 27–32 cells. $*p < 0.05$ and $**p < 0.01$. *p* values were calculated using Fisher's exact test. **C.** Representative contraction tracings recorded from CON, GC and EDMD iPSC-CMs. **D.** Violin graph to compare the peak height of the contraction among different groups in C. n = 77–102 cells. $***p < 0.001$ and $****p < 0.0001$. *p* values were calculated using One-way ANOVA tests. **E.** Mitochondrial ROS levels in CON, GC and EDMD iPSC-CMs. n = 3 independently biological repeats. $***p < 0.001$. *p* values were calculated using One-way ANOVA tests. Data is shown as mean ± sem. **F.** Western blot analysis of JAK2, p-STAT3 (727 and 705), STAT3, *p*-DRP1, and DPR1 expression in CON, GC and EDMD iPSC-CMs. **G.** Bar graphs to compare the protein expression in F. n = 6 independently biological repeats. $**p < 0.001$ and $****p < 0.0001$. *p* values were calculated using One-way ANOVA tests. Data is shown as mean ± sem. **H.** Representative graphs of co-staining of lamin A/C (red) and STAT3 (green) in CON, GC and EDMD iPSC-CMs. DAPI indicates nuclear staining (blue). White arrows indicate cells without nuclear localization of STAT3. Scale bar, 20 μm. **I.** Bar graph to compare the mean fluorescence intensity of STAT3 in the nucleus among different groups in H. n = 15 independently biological repeats. The $****p < 0.0001$. *p* values were calculated using One-way ANOVA tests. Data is shown as mean ± sem. **J.** Representative graphs of mitochondria in CON, GC and EDMD iPSC-CMs by staining of MitoTracker (Red). Hoechst indicates nuclear staining (blue). Scale bar, 10 μm. **K.** Bar graph to compare the mean branch diameter among different groups in J. n = 24 cells. $****p < 0.0001$. *p* values were calculated using One-way ANOVA tests. Data is shown as mean ± sem.

accessibility leading to the downregulation of *JAK2*, thus suppressing JAK2/STAT3 signaling in EDMD iPSC-CMs. Excessive oxidative stress, known as detrimental for both cardiomyocyte structure and function [37], ultimately then led to the predisposition towards arrhythmia and contractile dysfunction. The pathological contractile dysfunction phenotype, and the rescue effects of the activation of JAK2/STAT3, were both successfully verified using an EDMD patient-specific EHT model. Taken together, our findings indicate that the lamin A/C-JAK2/STAT3-ROS axis plays an essential role in regulating the pathophysiology of EDMD cardiac phenotypes (Fig. 7D).

Lamin A/C are pivotal structural proteins within the nucleus of the cell, forming the backbone of the nuclear lamina, a fibrous network that lines the interior of the nuclear envelope and which is essential for preserving the mechanical integrity of the nucleus [9,42]. These lamins also play a crucial role in various nuclear functions such as DNA replication, regulation of gene expression, and the cellular response to DNA damage [6–9,11,42]. Mutations in the genes encoding lamins A/C can result in proteins that fail to effectively perform their designated roles, thereby causing disruptions to the nuclear membrane's stability. As the nuclear envelope serves as a protective shield against external threats, this instability can render DNA more vulnerable to damage [6,8,11]. DNA damage acts as an intracellular stress signal that triggers a cascade of signaling pathways, including inflammatory responses [43]. When DNA damage and inflammation occur, these can impair mitochondrial function, potentially leading to metabolic disorders and disruption to the cell's normal operations [44]. This dysfunction may also result in an increased production of ROS [38], which, as highly reactive molecules, can cause damage to proteins, lipids, and DNA [45]. In this study, we have identified a pronounced pathogenic signature characterized by DNA damage and inflammatory activation in L204P iPSC-CMs. Concurrently, we observed impairments in mitochondrial function accompanied by an increase in ROS as the likely primary contributors to the observed resultant aberrant cardiac function.

The relevance of the observed suppression of JAK2 signaling in EDMD iPSC-CMs may also require some clarification. JAK2 is a component of the non-receptor tyrosine kinase JAK family. It plays a pivotal role in cellular proliferation, the progression through the cell cycle, the execution of apoptosis, the orchestration of mitotic recombination, the maintenance of genetic stability, and the modification of histones [24,25,31–34], exerting its influence on mitochondrial function predominantly through the regulation of STAT3 phosphorylation [28–30]. Upon phosphorylation, STAT3 dimerizes and translocates to the nucleus to modulate the transcription of target genes. Moreover, phosphorylated STAT3 is capable of directly entering mitochondria to modulate their energy metabolism [27]. The JAK2/STAT3 pathway is frequently triggered in response to inflammatory stimuli. For instance, IL-6 latches onto the IL-6 receptor, initiating a cascade that results in the activation of JAK2. This activated JAK2 subsequently phosphorylates STAT3, prompting it to phosphorylate and dimerize. Phosphorylated STAT3 dimers are then transported into the nucleus, where they orchestrate the transcription of specific target genes [24,26,46].

In spite of the inflammatory activation, and contrary to expectations, our experiments uncovered that the suppression of the JAK2/STAT3 pathway occurred together with a decreased rather than increased phosphorylation level of STAT3, as had also been previously reported [46]. In this, we must consider that mutations in the *LMNA* gene can disrupt the integrity of the nuclear envelope, which in turn affects chromatin organization and increases chromatin heterogeneity, ultimately leading to aberrant chromatin condensation. Such architectural alterations may act to modulate the accessibility of chromatin, thereby influencing the binding affinity of transcriptional regulatory proteins and impacting the ensuing regulation of downstream gene expression [42]. In our study, we utilized a comprehensive approach by integrating data from RNA-Seq and ATAC-Seq, which revealed diminished gene accessibility and a concomitant reduction in JAK2 expression levels. Moreover, pharmacological or genetic activation of JAK2/STAT3 significantly ameliorated the arrhythmic and contractile dysfunction phenotypes in L204P iPSC-CMs by improving mitochondrial function, highlighting the potential therapeutic avenue this approach represented for mitigating the cardiac effects of *LMNA* mutations.

LMNA-related cardiomyopathies display marked phenotypic variability attributable to diverse mutation sites, with their underlying pathogenic mechanisms intricately linked to the specific nature of each mutation. To date, the ClinVar database has documented over 500 pathogenic or likely pathogenic mutations within the *LMNA* gene. Pathogenic mechanisms underlying single-site mutations may therefore not fully account for the pathogenicity of all *LMNA* mutations. Given this limitation, systematic research on *LMNA* mutations becomes extremely important. In subsequent studies, we aim to conduct more in-depth explorations of different types of *LMNA* mutations, more thoroughly analyze their common and unique pathogenic mechanisms, and further verify the feasibility of relevant therapeutic targets.

One limitation in our study is the absence of the *in vivo* data. Further experiments using genetic animal models will be conducted to confirm our findings in the future investigations. A second limitation is that our findings are based only upon one single recruited *LMNA*-related EDMD patient. Once further cases of this rare genotype become apparent, we hope to facilitate further investigations among a broader patient cohort to confirm our findings.

In conclusion, our work unveils a novel mechanism involving chromatin compartment change-mediated suppression of the JAK2/STAT3 signaling pathway underlying the cardiac pathogenic phenotypes in *LMNA*-related EDMD. Our findings suggest that activation of JAK2/STAT3 could therefore serve as a potential novel therapeutic strategy for cardiac phenotypes associated with *LMNA*-related EDMD.

CRediT authorship contribution statement

Hangping Fan: Writing – original draft, Validation, Investigation, Formal analysis. **Zongkuai Yang:** Validation, Investigation, Formal analysis. **Hangying Ying:** Validation, Investigation, Formal analysis. **Jiuxiao Zhao:** Investigation, Formal analysis. **Xiaochen Wang:**

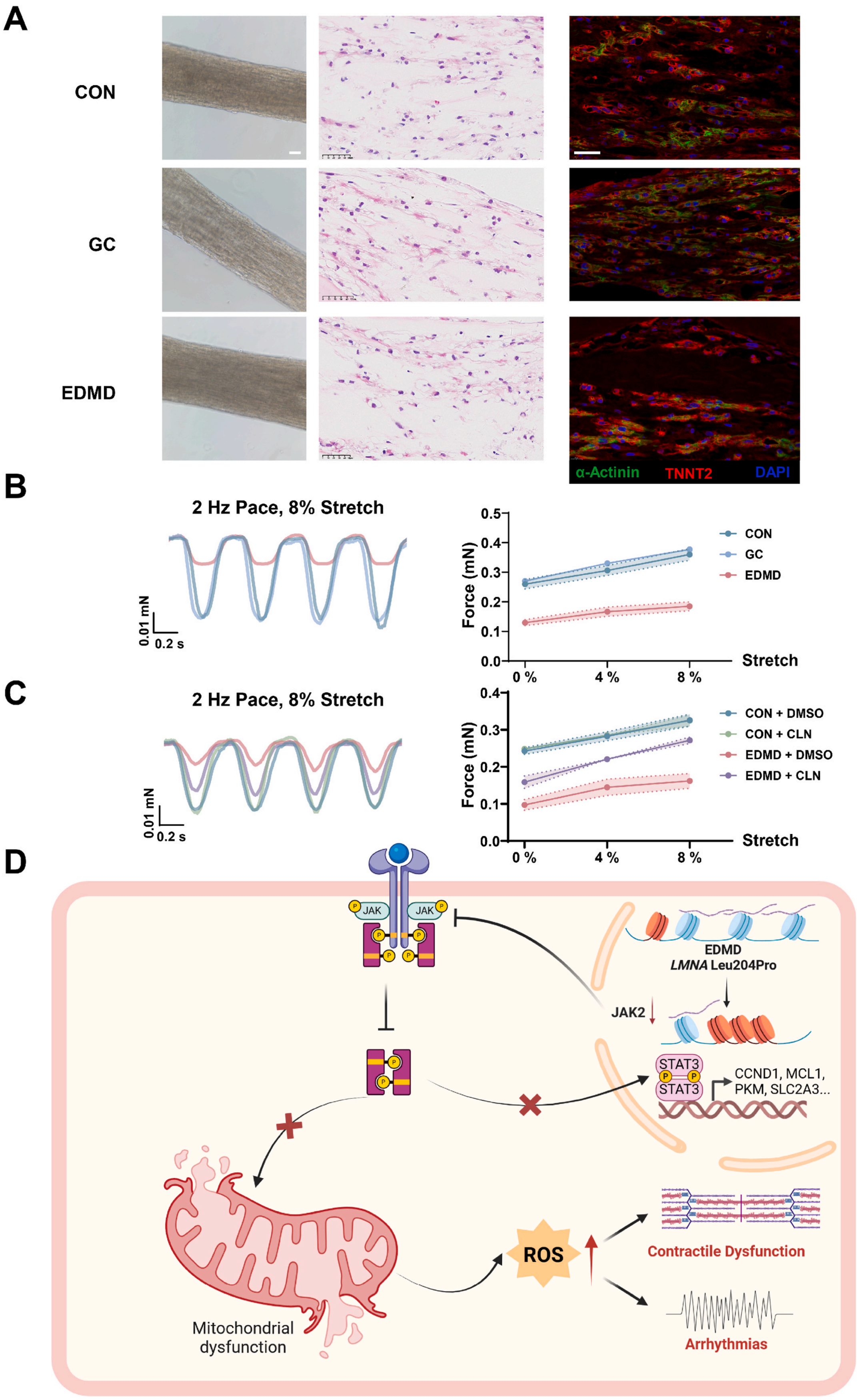

(caption on next page)

Fig. 7. Pharmacological activation of JAK2/STAT3 signaling improves the function of EDMD patient-specific EHTs. A. Representative longitudinal morphology of CON, GC and EDMD EHTs (scale bar, 100 μm) with H&E staining (scale bar, 50 μm) and TNNT2/α-Actinin/DAPI staining (scale bar, 50 μm). **B.** Representative contraction tracings recorded from CON, GC and EDMD EHTs under 2 Hz pacing and an 8 % stretching ratio. Line graph to compare the force among different groups in the left panel. n = 3 biological repeats. Data were shown as mean ± sem. **C.** Representative contraction tracings recorded from CON and EDMD EHTs with or without CLN treatment under 2 Hz pacing and an 8 % stretching ratio. Line graph to compare the force among different groups in the left panel. n = 5 biological repeats. Data were shown as mean ± sem. **D.** Proposed work model. EDMD patient-specific iPSC-CMs carrying the *LMNA* L204P mutation exhibit increased burdens of arrhythmia and contractile dysfunction. *LMNA* L204P decreases the chromatin opening and leads to the downregulation of *JAK2* in L204P iPSC-CMs. The deficiency of JAK2, in turn, results in reduced STAT3 activity. The suppression of the JAK2/STAT3 signaling pathway subsequently leads to impaired mitochondrial function and excessive ROS production, ultimately causing the observed arrhythmia and contractile dysfunction in L204P iPSC-CMs.

Validation, Project administration, Investigation, Funding acquisition, Formal analysis. **Junhao Gong:** Validation, Investigation. **Lingying Li:** Validation, Investigation. **Xujie Liu:** Validation, Investigation, Formal analysis. **Tingyu Gong:** Writing – review & editing, Supervision, Project administration, Investigation, Conceptualization. **Qing Ke:** Writing – review & editing, Supervision, Funding acquisition, Formal analysis, Conceptualization. **Lenan Zhuang:** Writing – review & editing, Supervision, Funding acquisition, Conceptualization. **Ping Liang:** Writing – review & editing, Supervision, Funding acquisition, Conceptualization.

Declaration of competing interest

The authors declare that they have no known competing financial interests or personal relationships that could have appeared to influence the work reported in this paper.

Acknowledgments

This work was supported by the “LingYan” Research and Development Project, China (2024C03155) (P.L.), the National Natural Science Foundation of China, China (82370354) (P.L.), the National Natural Science Foundation of China, China (82400372) (X.W.), the State Key Laboratory for Diagnosis and Treatment of Infectious Diseases, China (zz202402) (P.L.), the Natural Science Foundation of Zhejiang Province, China (LD21H020001) (P.L.), the National Key Research and Development Program of China, China (2017YFA0103700) (P.L.), the National Key Research and Development Program of China, China (2021YFA0805902) (L.Z.), the National Natural Science Foundation of China, China (32270884) (L.Z.), the Key Research and Development Program of Zhejiang, China (2023C03003) (Q.K.), and the Recruitment Program of Experts of Jiangxi Province, China (jxsq2023102164) (Q.K.).

Appendix A. Supplementary data

Supplementary data to this article can be found online at https://doi.org/10.1016/j.redox.2025.103638.

Data availability

Data will be made available on request.

References

[1] A.E. Emery, The muscular dystrophies, Lancet 359 (2002) 687–695, https://doi.org/10.1016/S0140-6736(02)07815-7.

[2] S.A. Heller, R. Shih, R. Kalra, P.B. Kang, Emery-Dreifuss muscular dystrophy, Muscle Nerve 61 (2020) 436–448, https://doi.org/10.1002/mus.26782.

[3] D. Kramarenko, R. Walsh, Emery–Dreifuss muscular dystrophy: a closer look at cardiac complications, Eur. Heart J. 44 (2023) 5074–5076, https://doi.org/10.1093/eurheartj/ehad735.

[4] B. Feingold, W.T. Mahle, S. Auerbach, P. Clemens, A.A. Domenighetti, J. L. Jefferies, D.P. Judge, A.K. Lal, L.W. Markham, W.J. Parks, T. Tsuda, P.J. Wang, S.-J. Yoo, Management of cardiac involvement associated with neuromuscular diseases: a scientific statement from the American heart association, Circulation 136 (2017), https://doi.org/10.1161/CIR.0000000000000526.

[5] A. Madej-Pilarczyk, Clinical aspects of Emery-Dreifuss muscular dystrophy, Nucleus 9 (2018) 314–320, https://doi.org/10.1080/19491034.2018.1462635.

[6] S.V. Ulianov, S.A. Doronin, E.E. Khrameeva, P.I. Kos, A.V. Luzhin, S.S. Starikov, A. A. Galitsyna, V.V. Nenasheva, A.A. Ilyin, I.M. Flyamer, E.A. Mikhaleva, M. D. Logacheva, M.S. Gelfand, A.V. Chertovich, A.A. Gavrilov, S.V. Razin, Y. Y. Shevelyov, Nuclear lamina integrity is required for proper spatial organization of chromatin in Drosophila, Nat. Commun. 10 (2019) 1176, https://doi.org/10.1038/s41467-019-09185-y.

[7] R. De Leeuw, Y. Gruenbaum, O. Medalia, Nuclear lamins: thin filaments with major functions, Trends Cell Biol. 28 (2018) 34–45, https://doi.org/10.1016/j.tcb.2017.08.004.

[8] Y. Gruenbaum, R. Foisner, Lamins: nuclear intermediate filament proteins with fundamental functions in nuclear mechanics and genome regulation, Annu. Rev. Biochem. 84 (2015) 131–164, https://doi.org/10.1146/annurev-biochem-060614-034115.

[9] J.M. Sobo, N.S. Alagna, S.X. Sun, K.L. Wilson, K.L. Reddy, Lamins: the backbone of the nucleocytoskeleton interface, Curr. Opin. Cell Biol. 86 (2024) 102313, https://doi.org/10.1016/j.ceb.2023.102313.

[10] M. Tatli, O. Medalia, Insight into the functional organization of nuclear lamins in health and disease, Curr. Opin. Cell Biol. 54 (2018) 72–79, https://doi.org/10.1016/j.ceb.2018.05.001.

[11] Y.Y. Shevelyov, S.V. Ulianov, The nuclear lamina as an organizer of chromosome architecture, Cells 8 (2019) 136, https://doi.org/10.3390/cells8020136.

[12] M.J. Stroud, I. Banerjee, J. Veevers, J. Chen, Linker of nucleoskeleton and cytoskeleton complex proteins in cardiac structure, function, and disease, Circ. Res. 114 (2014) 538–548, https://doi.org/10.1161/CIRCRESAHA.114.301236.

[13] R.M. McGillivary, D.A. Starr, G.W.G. Luxton, Building and breaking mechanical bridges between the nucleus and cytoskeleton: regulation of LINC complex assembly and disassembly, Curr. Opin. Cell Biol. 85 (2023) 102260, https://doi.org/10.1016/j.ceb.2023.102260.

[14] I. Andreu, I. Granero-Moya, N.R. Chahare, K. Clein, M. Molina-Jordán, A.E. M. Beedle, A. Elosegui-Artola, J.F. Abenza, L. Rossetti, X. Trepat, B. Raveh, P. Roca-Cusachs, Mechanical force application to the nucleus regulates nucleocytoplasmic transport, Nat. Cell Biol. 24 (2022) 896–905, https://doi.org/10.1038/s41556-022-00927-7.

[15] X. Di, X. Gao, L. Peng, J. Ai, X. Jin, S. Qi, H. Li, K. Wang, D. Luo, Cellular mechanotransduction in health and diseases: from molecular mechanism to therapeutic targets, Signal Transduct Target Ther 8 (2023) 282, https://doi.org/10.1038/s41392-023-01501-9.

[16] M. Maurer, J. Lammerding, The driving force: nuclear mechanotransduction in cellular function, fate, and disease, Annu. Rev. Biomed. Eng. 21 (2019) 443–468, https://doi.org/10.1146/annurev-bioeng-060418-052139.

[17] I.P. Uray, K. Uray, Mechanotransduction at the plasma membrane-cytoskeleton interface, Int. J. Mol. Sci. 22 (2021) 11566, https://doi.org/10.3390/ijms222111566.

[18] A.A. Khilan, N.A. Al-Maslamani, H.F. Horn, Cell stretchers and the LINC complex in mechanotransduction, Arch. Biochem. Biophys. 702 (2021) 108829, https://doi.org/10.1016/j.abb.2021.108829.

[19] S. Dupont, S.A. Wickström, Mechanical regulation of chromatin and transcription, Nat. Rev. Genet. 23 (2022) 624–643, https://doi.org/10.1038/s41576-022-00493-6.

[20] J. Lee, V. Termglinchan, S. Diecke, I. Itzhaki, C.K. Lam, P. Garg, E. Lau, M. Greenhaw, T. Seeger, H. Wu, J.Z. Zhang, X. Chen, I.P. Gil, M. Ameen, K. Sallam, J.-W. Rhee, J.M. Churko, R. Chaudhary, T. Chour, P.J. Wang, M.P. Snyder, H. Y. Chang, I. Karakikes, J.C. Wu, Activation of PDGF pathway links LMNA mutation to dilated cardiomyopathy, Nature 572 (2019) 335–340, https://doi.org/10.1038/s41586-019-1406-x.

[21] A. Bertero, P.A. Fields, A.S.T. Smith, A. Leonard, K. Beussman, N.J. Sniadecki, D.-H. Kim, H.-F. Tse, L. Pabon, J. Shendure, W.S. Noble, C.E. Murry, Chromatin compartment dynamics in a haploinsufficient model of cardiac laminopathy, JCB (J. Cell Biol.) 218 (2019) 2919–2944, https://doi.org/10.1083/jcb.201902117.

[22] Y. Wang, A. Elsherbiny, L. Kessler, J. Cordero, H. Shi, H. Serke, O. Lityagina, F. A. Trogisch, M.M. Mohammadi, I. El-Battrawy, J. Backs, T. Wieland, J. Heineke, G. Dobreva, Lamin A/C-dependent chromatin architecture safeguards naïve pluripotency to prevent aberrant cardiovascular cell fate and function, Nat. Commun. 13 (2022) 6663, https://doi.org/10.1038/s41467-022-34366-7.

[23] S. Maynard, A. Hall, P. Galanos, S. Rizza, T. Yamamoto, H.H. Gram, S.H.N. Munk, M. Shoaib, C.S. Sørensen, V.A. Bohr, M. Lerdrup, A. Maya-Mendoza, J. Bartek, Lamin A/C impairments cause mitochondrial dysfunction by attenuating PGC1α and the NAMPT-NAD+ pathway, Nucleic Acids Res. 50 (2022) 9948–9965, https://doi.org/10.1093/nar/gkac741.

[24] A. Sarapultsev, E. Gusev, M. Komelkova, I. Utepova, S. Luo, D. Hu, JAK-STAT signaling in inflammation and stress-related diseases: implications for therapeutic interventions, Mol Biomed 4 (2023) 40, https://doi.org/10.1186/s43556-023-00151-1.

[25] Y. Zhong, B. Yin, Y. Ye, O.Y.A.T. Dekhel, X. Xiong, Z. Jian, L. Gu, The bidirectional role of the JAK2/STAT3 signaling pathway and related mechanisms in cerebral

ischemia-reperfusion injury, Exp. Neurol. 341 (2021) 113690, https://doi.org/10.1016/j.expneurol.2021.113690.

[26] J. Huynh, A. Chand, D. Gough, M. Ernst, Therapeutically exploiting STAT3 activity in cancer - using tissue repair as a road map, Nat. Rev. Cancer 19 (2019) 82–96, https://doi.org/10.1038/s41568-018-0090-8.

[27] J. Wegrzyn, R. Potla, Y.-J. Chwae, N.B.V. Sepuri, Q. Zhang, T. Koeck, M. Derecka, K. Szczepanek, M. Szelag, A. Gornicka, A. Moh, S. Moghaddas, Q. Chen, S. Bobbili, J. Cichy, J. Dulak, D.P. Baker, A. Wolfman, D. Stuehr, M.O. Hassan, X.-Y. Fu, N. Avadhani, J.I. Drake, P. Fawcett, E.J. Lesnefsky, A.C. Larner, Function of mitochondrial Stat3 in cellular respiration, Science 323 (2009) 793–797, https://doi.org/10.1126/science.1164551.

[28] S. Comità, S. Femmino, C. Thairi, G. Alloatti, K. Boengler, P. Pagliaro, C. Penna, Regulation of STAT3 and its role in cardioprotection by conditioning: focus on non-genomic roles targeting mitochondrial function, Basic Res. Cardiol. 116 (2021) 56, https://doi.org/10.1007/s00395-021-00898-0.

[29] Z. Harhous, G.W. Booz, M. Ovize, G. Bidaux, M. Kurdi, An update on the multifaceted roles of STAT3 in the heart, Front. Cardiovasc. Med. 6 (2019) 150, https://doi.org/10.3389/fcvm.2019.00150.

[30] J.A. Meier, A.C. Larner, Toward a new STATe: the role of STATs in mitochondrial function, Semin. Immunol. 26 (2014) 20–28, https://doi.org/10.1016/j.smim.2013.12.005.

[31] S.P. Barry, P.A. Townsend, D.S. Latchman, A. Stephanou, Role of the JAK-STAT pathway in myocardial injury, Trends Mol. Med. 13 (2007) 82–89, https://doi.org/10.1016/j.molmed.2006.12.002.

[32] R. Bolli, B. Dawn, Y.-T. Xuan, Role of the JAK-STAT pathway in protection against myocardial ischemia/reperfusion injury, Trends Cardiovasc. Med. 13 (2003) 72–79, https://doi.org/10.1016/s1050-1738(02)00230-x.

[33] K. Boengler, D. Hilfiker-Kleiner, H. Drexler, G. Heusch, R. Schulz, The myocardial JAK/STAT pathway: from protection to failure, Pharmacol. Ther. 120 (2008) 172–185, https://doi.org/10.1016/j.pharmthera.2008.08.002.

[34] E. Mascareno, M. El-Shafei, N. Maulik, M. Sato, Y. Guo, D.K. Das, M.A. Siddiqui, JAK/STAT signaling is associated with cardiac dysfunction during ischemia and reperfusion, Circulation 104 (2001) 325–329, https://doi.org/10.1161/01.cir.104.3.325.

[35] F.A. Ran, P.D. Hsu, J. Wright, V. Agarwala, D.A. Scott, F. Zhang, Genome engineering using the CRISPR-Cas9 system, Nat. Protoc. 8 (2013) 2281–2308, https://doi.org/10.1038/nprot.2013.143.

[36] L. Yang, M. Guell, S. Byrne, J.L. Yang, A. De Los Angeles, P. Mali, J. Aach, C. Kim-Kiselak, A.W. Briggs, X. Rios, P.-Y. Huang, G. Daley, G. Church, Optimization of scarless human stem cell genome editing, Nucleic Acids Res. 41 (2013) 9049–9061, https://doi.org/10.1093/nar/gkt555.

[37] B. Zhou, R. Tian, Mitochondrial dysfunction in pathophysiology of heart failure, J. Clin. Investig. 128 (2018) 3716–3726, https://doi.org/10.1172/JCI120849.

[38] D.B. Zorov, M. Juhaszova, S.J. Sollott, Mitochondrial reactive oxygen species (ROS) and ROS-induced ROS release, Physiol. Rev. 94 (2014) 909–950, https://doi.org/10.1152/physrev.00026.2013.

[39] E. Bertero, C. Maack, Calcium signaling and reactive oxygen species in mitochondria, Circ. Res. 122 (2018) 1460–1478, https://doi.org/10.1161/CIRCRESAHA.118.310082.

[40] A. Görlach, K. Bertram, S. Hudecova, O. Krizanova, Calcium and ROS: a mutual interplay, Redox Biol. 6 (2015) 260–271, https://doi.org/10.1016/j.redox.2015.08.010.

[41] G. Favaro, V. Romanello, T. Varanita, M. Andrea Desbats, V. Morbidoni, C. Tezze, M. Albiero, M. Canato, G. Gherardi, D. De Stefani, C. Mammucari, B. Blaauw, S. Boncompagni, F. Protasi, C. Reggiani, L. Scorrano, L. Salviati, M. Sandri, DRP1-mediated mitochondrial shape controls calcium homeostasis and muscle mass, Nat. Commun. 10 (2019) 2576, https://doi.org/10.1038/s41467-019-10226-9.

[42] K. Piekarowicz, M. Machowska, E. Dratkiewicz, D. Lorek, A. Madej-Pilarczyk, R. Rzepecki, The effect of the lamin A and its mutants on nuclear structure, cell proliferation, protein stability, and mobility in embryonic cells, Chromosoma 126 (2017) 501–517, https://doi.org/10.1007/s00412-016-0610-9.

[43] Y. Zhao, M. Simon, A. Seluanov, V. Gorbunova, DNA damage and repair in age-related inflammation, Nat. Rev. Immunol. 23 (2023) 75–89, https://doi.org/10.1038/s41577-022-00751-y.

[44] C.S. Dela Cruz, M.-J. Kang, Mitochondrial dysfunction and damage associated molecular patterns (DAMPs) in chronic inflammatory diseases, Mitochondrion 41 (2018) 37–44, https://doi.org/10.1016/j.mito.2017.12.001.

[45] L.L. Camargo, F.J. Rios, A.C. Montezano, R.M. Touyz, Reactive oxygen species in hypertension, Nat. Rev. Cardiol. 22 (2025) 20–37, https://doi.org/10.1038/s41569-024-01062-6.

[46] Y. Jin, Y. Kang, M. Wang, B. Wu, B. Su, H. Yin, Y. Tang, Q. Li, W. Wei, Q. Mei, G. Hu, V. Lukacs-Kornek, J. Li, K. Wu, X. Yuan, W. Wang, Targeting polarized phenotype of microglia via IL6/JAK2/STAT3 signaling to reduce NSCLC brain metastasis, Signal Transduct Target Ther 7 (2022) 52, https://doi.org/10.1038/s41392-022-00872-9.